Estimates of κ_0 and Effects on Ground Motions in the San Francisco Bay Area

Tara Nye*[1], Valerie J. Sahakian[1], Elias King[1,2], Annemarie Baltay[3], and Alexis Klimasewski[1,4]

ABSTRACT

Ground-motion studies are a key component of seismic hazard analyses and often rely on information of the source, path, and site. Extensive research has been done on each of these parameters; however, site-specific studies are of particular interest to seismic hazard studies, especially in the field of earthquake engineering, as near-site conditions can have a significant impact on the resulting ground motion at a site. There has been much focus on the constraint of site parameters and their application to seismic hazard studies, especially in the development of ground-motion models (GMMs). Kappa is an observational parameter describing the high-frequency attenuation of spectra, and its site contribution (κ_0) has shown to be a good predictor of high-frequency ground motions; however, measurements are often limited. In this study, we develop a κ_0 dataset for the San Francisco Bay area (SFBA) by estimating κ_0 for 228 stations, and we produce a continuous regional map of κ_0. We find κ_0 to range between 0.003 and 0.072 s, with larger values concentrating on the east, north, and south sides of the bay, and lower values concentrating on the west side. We also evaluate the robustness of κ_0 as a site parameter and find it to correlate with peak ground acceleration. These estimates of κ_0 can add predictive power to GMMs, thus increasing the accuracy of predicted ground motion and improving the robustness of ground-motion studies in the SFBA.

KEY POINTS

- The parameter κ_0 is an important predictor of local earthquake ground motions but requires empirical studies.
- Regional values of κ_0 correlate well with local geology and adequately represent peak ground acceleration.
- Our results can be used to better constrain ground-motion model site effects, thus improving hazard estimates.

Supplemental Material

INTRODUCTION

Kappa (κ) is an observational spectral parameter that describes the high-frequency decay of *S*-wave acceleration spectra (Anderson and Hough, 1984). Considered to be controlled mainly by site characteristics, κ can be a valuable parameter to characterize high-frequency site conditions, which are critical to earthquake engineering and seismic hazards studies. In the past decade, some empirical ground-motion models (GMMs) have incorporated κ as a site parameter (Laurendeau *et al.*, 2013; Hassani and Atkinson, 2018). Synthetic GMMs, a necessary supplement for regions lacking frequent events or seismic instrumentation, have applied κ as a parameter for high-frequency attenuation with various stochastic methods (e.g., Boore, 2003; Graves and Pitarka, 2004; Motazedian and Atkinson, 2005; Somerville *et al.*, 2009; Mai *et al.*, 2010). In addition, κ is often used for host-to-site adjustments in empirical GMMs, which adjust modeled ground motion using an average regional κ-value for the study region (Douglas, 2006; Van Houtte *et al.*, 2011; Biro and Renault, 2012). Although such studies have not been performed yet, κ could also be used to help constrain regional velocity models, as greater-attenuating media are likely correlated with weaker, low-velocity zones (Gordon and Davis, 1968; Hough *et al.*, 1999; Dalton *et al.*, 2009).

κ_0 can be empirically determined but does require many earthquakes recorded on each seismic station of interest. The San Francisco Bay area (SFBA) is a seismically active region with a dense seismic network (Fig. 1); however, no such κ_0 models exist here. The main objectives for this study are to (1) model κ_0 in the SFBA using a dense network of seismic stations and (2) evaluate how well the model represents ground motions and site effects in this region. We also aim to relate these

1. Department of Earth Sciences, University of Oregon, Eugene, Oregon, U.S.A., https://orcid.org/0000-0003-3210-6013 (TN); https://orcid.org/0000-0002-3278-4458 (VJS); https://orcid.org/0000-0002-0433-0723 (AK); 2. Now at Nanohmics, Austin, Texas, U.S.A.; 3. U.S. Geological Survey, Earthquake Science Center, Moffett Field, California, U.S.A., https://orcid.org/0000-0002-6514-852X (AB); 4. Now at Agrograph, Madison, Wisconsin, U.S.A.

*Corresponding author: tnye@uoregon.edu

Cite this article as Nye, T., V. J. Sahakian, E. King, A. Baltay, and A. Klimasewski (2022). Estimates of κ_0 and Effects on Ground Motions in the San Francisco Bay Area, *Bull. Seismol. Soc. Am.* **XX**, 1–20, doi: 10.1785/0120220046

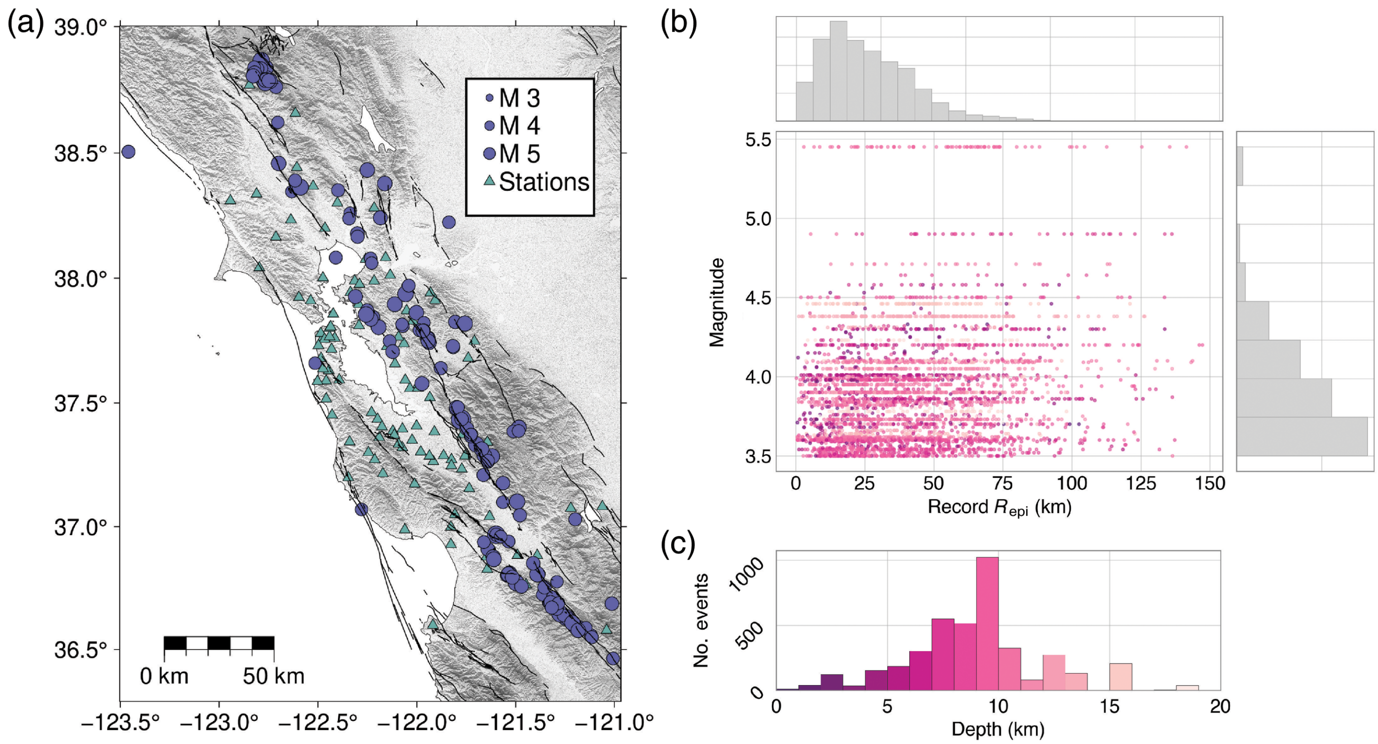

Figure 1. (a) Study region of the San Francisco Bay area (SFBA) with events (circles) and seismic stations (triangles) used to estimate κ_0. Quaternary faults are represented by solid black lines. (b) Magnitude and epicentral distance (R_{epi}) distribution of records used in this study are colored by depth. (c) Depth distribution of records used. The color version of this figure is available only in the electronic edition.

modeled parameters with known geologic features to further constrain the subsurface geology of the SFBA.

Finally, because κ is estimated from seismic records, its spatial measurement is biased by the location of seismic stations. Subsequently, its utility for region-specific or spatially varying (i.e., nonergodic) GMMs (e.g., Landwehr *et al.*, 2016) is limited. Producing a regional map of κ_0 will not only support the development of nonergodic GMMs but will also be useful for ground-motion seismology studies in regions lacking seismic instrumentation. To our knowledge, only two continuous maps of κ_0 have been developed at the time of this publication: New Zealand (Van Houtte *et al.*, 2018) and Europe (Pilz *et al.*, 2019). However, both the maps are intended to represent hard-rock conditions only. Our final product is a spatially continuous map of κ_0 in the SFBA, representing a spectrum of site conditions (Nye *et al.*, 2022b), which will be a valuable contribution to the U.S. Geological Survey (USGS) Bay area velocity model shallow layer (Brocher *et al.*, 2006; Jachens *et al.*, 2006; Rodgers *et al.*, 2020; Aagaard and Hirakawa, 2021).

BACKGROUND

The theoretical ϖ^2 earthquake source model assumes a flat spectral acceleration response at frequencies higher than the corner frequency (Brune, 1970). However, empirical observations demonstrate additional attenuation in the high-frequency range above the transitional frequency f_{max} typically above the corner frequency f_c (Hanks, 1982). Assuming a flat site spectrum (i.e., no amplification), Anderson and Hough (1984) first defined κ as a way to quantify this deviation of observed spectra from the theoretical ϖ^2 source model by fitting the decay of the high-frequency portion of acceleration spectra:

$$A(f) = A_0 \exp(-\pi\kappa f), \quad (1)$$

in which f denotes the frequency, A_0 is an amplitude parameter dependent on the source and path, and κ describes the slope of the decay in linear-log space.

As κ is estimated from seismic recordings, it describes an observation rather than a driving mechanism. Although κ can be related to physical parameters, there has been much debate on its origins, especially its association with source, path, and site effects. Many studies have examined the path dependency of κ (e.g., Anderson and Hough, 1984; Anderson, 1991; Fernández *et al.*, 2010; Kilb *et al.*, 2012; Ktenidou *et al.*, 2013; Castro and Ávila-Barrientos, 2015; Castro *et al.*, 2022). There has also been discussion over whether κ is a product of the source or site, as κ signifies a relative depletion of high frequencies, which could be due to attenuation or a source deficiency. A handful of studies address possible source mechanisms, such as nonelasticity of the fault (Papageorgiou and Aki, 1983) or a tectonic region dependency (Ktenidou *et al.*, 2013). However, κ has been shown to have no magnitude dependence (Anderson, 1986; Fernández *et al.*, 2010; Ktenidou *et al.*, 2013; Castro and Ávila-Barrientos, 2015; Haendel *et al.*, 2020). Ultimately, it is largely accepted that κ is influenced mainly by near-site geologic conditions and to a lesser degree by the path and source. κ typically increases with distance, because it is influenced by the overall path attenuation (i.e., Q-profile), and scatter in κ-values at a site from nearby events is likely due to varying source properties (Kilb *et al.*, 2012).

Of particular interest is κ's ability to predict ground-motion site characteristics, given its local control on the high-frequency content of seismic recordings. GMMs approximate shaking intensity from earthquakes based on a set of independent parameters, which describe the earthquake source, attenuation, and site effects (Douglas and Edwards, 2016). Site characterization is a key component of these GMMs, as site conditions are more easily measurable and can have a large effect on the local ground shaking. V_{S30}, the time-averaged shear-wave velocity in the upper 30 m of crust, is a common site parameter in GMMs (e.g., Boore *et al.*, 1993; Borcherdt, 1994; Campbell and Bozorgnia, 2008; Bayless and Abrahamson, 2018) because of its large-scale proxy-based availability and its representation of local amplification. It is, however, a poorly constrained parameter as direct measurements of V_{S30} are less abundant, and thus V_{S30} is often inferred from local geology. Estimated V_{S30} data can vary up to 50% from true V_{S30}, which can have a significant effect on ground-motion studies (Ktenidou *et al.*, 2014). κ, however, has shown to be a similar or better predictor of certain high-frequency ground motions due to site effects and should also be considered in GMMs (Silva and Darragh, 1995; Klimasewski *et al.*, 2019, 2021). Relationships between κ and V_{S30} are, however, desirable for instances where measured κ-values may not exist but are still required for GMMs.

In ergodic GMMs, average regional conditions are assumed to be representative of all local conditions (Douglas and Edwards, 2016). Although reasonable to a degree, there can still be vast variability over a small scale. Moreover, although modern ergodic GMMs are developed with site terms, application of these models requires site-specific parameters, which can be limited to locations of seismic instruments. To apply these models to any location, partially or fully nonergodic models are needed. The use of nonergodic, fully spatially varying models provides more accurate predictions and could reduce aleatory variability (Al Atik *et al.*, 2014; Douglas and Edwards, 2016; Stewart *et al.*, 2019), even up to ∼40% (Landwehr *et al.*, 2016). However, such models require the availability of spatially varying parameters, which motivates this study's objective to produce a regional map of κ_0.

DATA AND METHODS

Dataset

To compute κ_0 values in the SFBA, we use a dataset of approximately 11,000 three-component earthquake acceleration recordings from 227 events in the SFBA region that occurred between 2000 and 2021 (Fig. 1a). Because this method requires a substantial frequency range above the corner frequency with which to solve for κ, we limit our dataset to include only earthquakes with a moment magnitude (**M**) ≥ 3.5. We also limit our dataset to records recorded at distances (R_{epi}, epicentral distance) ≤ 150 km to reduce bias from longer travel time in the subsurface and varying Q-structure at greater depths (Hough and Anderson, 1988; Ji *et al.*, 2022). Most of the events in our dataset are 3.5 < **M** < 4, with the largest being **M** 5.5 (Fig. 1b). The majority of earthquakes were reported in moment magnitude, with the exceptions of 12 events reported in local magnitude (M_L) and two in duration magnitude (M_D); the local magnitudes are assumed to be the same as moment magnitude in this range (Ross *et al.*, 2016). The earthquakes were recorded on 228 stations: 15 broadband velocity stations from the Berkeley Digital Seismic (BK) network and 213 accelerometers from the BK, Berkeley Geysers (BG), USGS Northern California Regional (NC), National Strong Motion Project (NP), and California Department of Water (WR) networks.

All data were high-pass filtered at 0.28 Hz to filter out a microseism, demeaned, baseline-corrected, and corrected for instrument response with output units in acceleration (m/s^2). To maintain sufficient quality data for our inversions, all recordings have the minimum signal-to-noise ratio (SNR) of 3 (Ktenidou *et al.*, 2013) across the high-frequency range of 10–30 Hz, across the whole spectrum, and in the time domain. We not only retain records with an SNR ≥ 3 for all scenarios to avoid high-frequency noise that could contaminate κ estimates, but we also use the whole spectrum in horizontal-to-vertical spectral ratio (HVSR) calculations. We also want to eliminate records that may have a significant SNR in the frequency domain but are noisy in the time domain.

Frequency domain SNR is calculated as the mean of the signal spectrum divided by the mean of the noise spectrum. We define the noise as the first 6–8 s of useable record (i.e., unaffected by the cosine taper in removal of instrument response), depending on how long the pre-*P*-arrival record is. If less than 6 s are available, the last 8 s of the coda are used (Ktenidou *et al.*, 2016). We define the signal as an equivalent number of seconds following the theoretical *S*-wave arrival (assuming 3.5 km/s average *S*-wave velocity). Time domain SNR is calculated as the ratio of the standard deviation of signal to the standard deviation of noise, using the same time windows as previously described. The size of our dataset does not contain all available recordings from the SFBA that meet these criteria, as we have culled our dataset to only use recordings from stations that have at least eight useable records to solve for κ to improve the robustness of our estimates. This is further explained in the Estimating site kappa section.

κ is calculated from the *S*-wave contribution to acceleration spectra (Anderson and Hough, 1984). However, several studies show the signal window has little effect on the results of κ, provided that the energetic part of the *S* wave is preserved (Anderson and Hough, 1984; Van Houtte *et al.*, 2011). To ensure this, our seismograms are trimmed to 2 s before the theoretical *S*-wave arrival and are cut at variable times after, depending on the energy content of the records. The upper time limit is the maximum time at which 80% of the Arias intensity (representative of total energy) is met for the three components of each record (Fernández *et al.*, 2010; Van Houtte *et al.*, 2011). We obtain the Fourier amplitude spectra (FAS) for each horizontal component using mtspec (Prieto *et al.*, 2009; Krischer, 2016), which also returns the jackknife 5% and 95% confidence intervals. We then obtain the orientation-independent vector sum (equation 2) of each recording's horizontal components (Ktenidou *et al.*, 2016), and the error from mtspec is propagated into the inversion for κ on the averaged spectra. The equation for the vector sum is provided subsequently, in which $A_{VS}(f)$ denotes the vector sum amplitude as a function of frequency (f), and H_1 and H_2 are the horizontal components:

$$A_{VS}(f) = \sqrt{H_1(f)^2 + H_2(f)^2}. \tag{2}$$

Estimating site kappa

Individual record kappa. Various methods have been used to measure κ, often taking a record-by-record approach, such as the widely used method of performing a linear least-squares fit to the high-frequency decay of *S*-wave acceleration spectra (e.g., Anderson and Hough, 1984; Purvance and Anderson, 2003; Douglas *et al.*, 2010; Fernández *et al.*, 2010; Van Houtte *et al.*, 2018 ,2014 ,2011; Ktenidou *et al.*, 2013, 2015; Askan *et al.*, 2014; Castro and Ávila-Barrientos, 2015; Ktenidou and Abrahamson, 2016; Palmer and Atkinson, 2020; Xu *et al.*, 2020; Ji *et al.*, 2021, 2022; Castro *et al.*, 2022). Other record-by-record methods include solving for M_0, f_0, and κ by minimizing the root mean square misfit between the observed and theoretical spectra (Anderson and Humphrey, 1991; Humphrey and Anderson, 1992), solving for κ on the low-frequency slope of small-magnitude ($M_L < 1$) displacement spectra (Biasi and Smith, 2001; Kilb *et al.*, 2012), and fixing the stress drop and using M_0 and f_0 to solve for κ (Kilb *et al.*, 2012). Spectral decomposition, a method in which a large suite of records is used to deconvolve source and site spectra, has also been used to solve for κ on the site spectra (Klimasewski *et al.*, 2019). This is not the full list of methods. For a more complete summary, see Ktenidou *et al.* (2014).

We follow the traditional method of Anderson and Hough (1984) to perform a least-squares fit on a high-frequency range ($f_e < f < f_x$) of the acceleration spectra in linear–log space, in which f_e is some frequency well-above the corner frequency, and f_x is the noise floor of the spectrum. Anderson and Hough (1984) mainly applied this method to a dataset with events **M** 5 +. There has been some debate around applying this method to smaller magnitudes, as these events typically have a higher corner frequency, resulting in possible source effect contamination. However, Kilb *et al.* (2012) suggest that this is mainly an issue for smaller events (**M** < 3.5) that exist below our magnitude range, and several studies have successfully applied this method with events in our magnitude range (e.g., Van Houtte *et al.*, 2011; Ktenidou *et al.*, 2013, 2015). The events in our study have an approximate expected corner frequency of 0.5–5 Hz, which is well below the high-frequency range typically used to solve for κ. We thus assume this method to be suitable for our dataset and have carefully chosen frequency ranges that are sufficiently above the earthquake corner frequencies.

Frequency range selection. Most κ studies have manually picked the frequency ranges for each record. However, considering the large number of records used in this study (over 10,000), we have developed an algorithm to select the lower and upper frequency bounds on each record that is two stage. (1) Prior to selecting f_e and f_x on each record, we determine the maximum limits for the frequency bounds that are influenced by the (a) corner frequency, (b) instrument response, and (c) possible site amplification. (2) The frequency bounds f_e and f_x are selected based on characteristics of the first derivative of a degree 15 polynomial fit to each record spectrum (Fig. 2).

A key assumption in solving for κ is that the high-frequency decay is isolated from source effects (Anderson and Hough, 1984). In step 1a of the algorithm, we account for this by imposing a lower limit of 1.5 times the theoretical corner frequency (f_c) (Ktenidou *et al.*, 2016), which is derived using the following equation from Hanks and Thatcher (1972):

$$f_c = \beta\left(\frac{\Delta\sigma}{8.47M_0}\right)^{1/3}. \tag{3}$$

The seismic moment (M_0) is obtained using the moment magnitude of each event and the Hanks and Kanamori (1979) relation. We assume an average regional *S*-wave velocity (β) of 3.5 km/s and an average stress drop ($\Delta\sigma$) of 5 MPa (Atkinson and Beresnev, 1997; Baltay and Hanks, 2014). To address the instrument response in step 1b of our algorithm, an upper limit of 80% of the Nyquist frequency is set for lower sampling rate (e.g., 50, 80 Hz) stations; but we impose a 35 Hz limit for higher sampling rate stations, as this is the smallest maximum value of flat instrument response for such stations (Van Houtte *et al.*, 2014).

The presence of site amplification can bias κ estimates, especially if the fundamental frequency falls within the frequency range of interest (Parolai and Bindi, 2004; Ktenidou *et al.*, 2016). As the SFBA is covered by considerable weak material in the shallow subsurface, this is a possible concern for our dataset. In step 1c of our algorithm, we minimize the effects of site amplification in solving for κ by computing the average earthquake-based HVSR (eHVSR) at each site (Lermo and Chávez-García, 1993; Ktenidou *et al.*, 2016; Ito *et al.*, 2020). For each site eHVSR curve, we manually select frequency

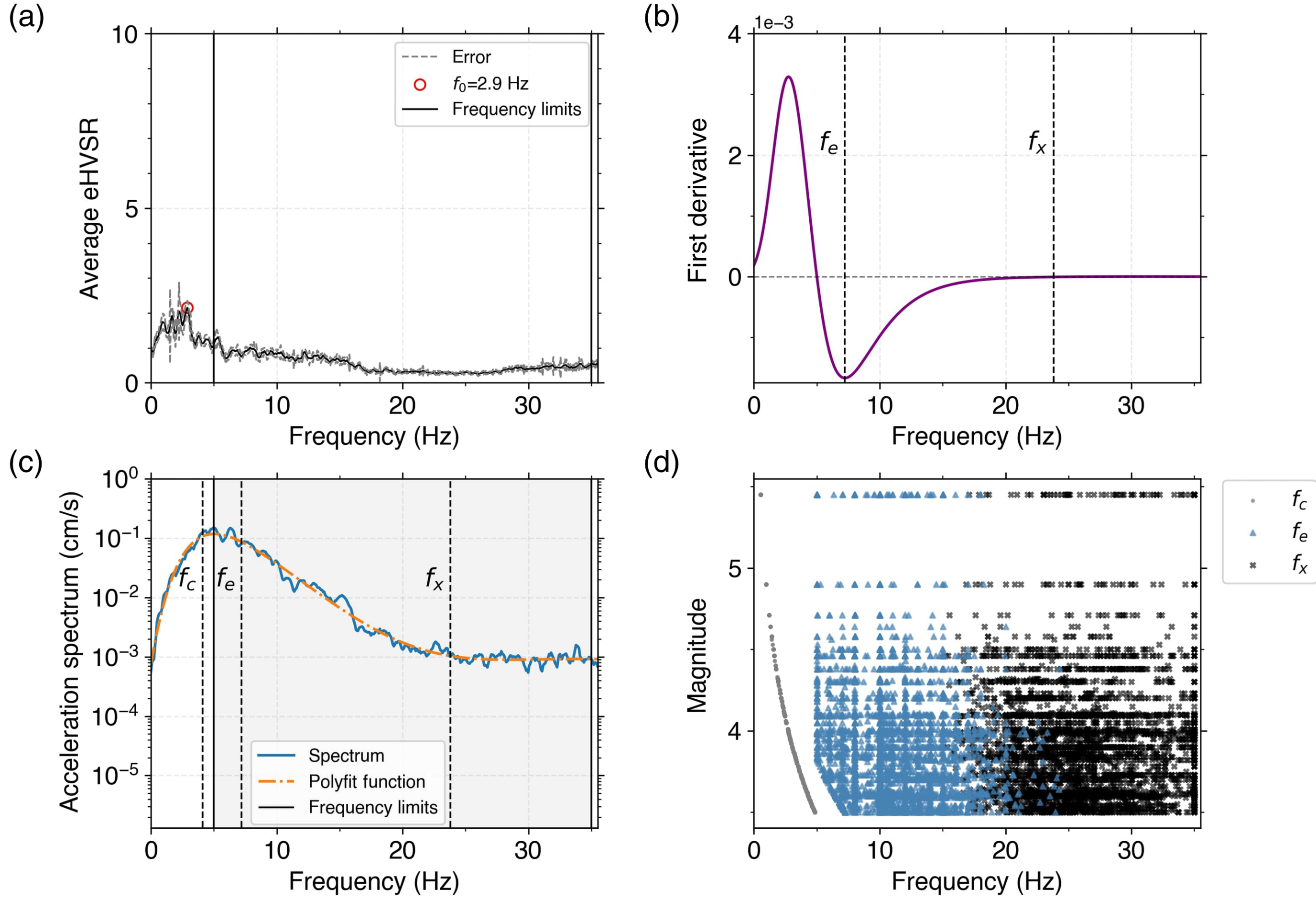

Figure 2. Example application of the algorithm to select the frequency ranges f_e and f_x used to solve for κ on an individual record. (a) Average earthquake-based horizontal-to-vertical spectral ratio (eHVSR) for station J030 with the fundamental frequency (f_0) indicated by a red circle, and the manually selected frequency limits indicated solid black lines. (b) First derivative of the polyfit function in (c). f_e is the frequency at which the first derivative is the lowest, and f_x is the frequency at which the first derivative reaches a threshold value of 8×10^{-5}. (c) Example record spectrum for station J030 with a degree 15 polyfit function fit to the spectrum. f_c indicates the theoretical corner frequency of this event, and f_e and f_x are the frequency bounds determined in (b). The shaded region indicates the maximum frequency limits bounded by the eHVSR frequencies (solid black lines) from (a). (d) Distribution of f_c, f_e, and f_x for all records in the dataset as a function of earthquake magnitude. The color version of this figure is available only in the electronic edition.

ranges that bound a generally flat portion of the curve, regardless of the true amplitude of the eHVSR (Ktenidou *et al.*, 2016). These frequency ranges serve as the maximum limits to f_e and f_x (see Fig. S1, for example eHVSR curves or the online Zenodo dataset, Nye *et al.*, 2022b, for the full set of stations). We compute site eHVSR using three-component *S*-wave records by first smoothing the waveforms with a Hanning filter (Çelebi *et al.*, 2018) and then calculating the spectra using mtspec—a Python wrapper for the Multitaper Spectrum Estimation Library (Prieto *et al.*, 2009; Krischer, 2016). The horizontal spectral components for each recording are geometrically averaged and divided by the vertical component, resulting in an eHVSR for each recording. The eHVSR records for each site are averaged in logarithmic space to obtain an average eHVSR site spectrum (Ito *et al.*, 2020). We recognize that the eHVSR is not a true site amplification transfer function, but rather a simplistic approach that provides some insight into the amplifying conditions and helps further constrain the part of the spectrum dominated by site attenuation.

After determining the maximum frequency limits, f_e and f_x are selected in step 2 of our algorithm based on the first derivative of a degree 15 polynomial fit to each spectrum. The lower bound f_e is the frequency of the minimum of the first derivative, as this indicates the steepest negative slope of the spectrum. The upper bound f_x is the frequency at which the first derivative reaches an arbitrary threshold of -8×10^{-5} (Fig. 2b), assuming data units of centimeters per square second. This indicates the relative frequency at which most of the spectral records in our dataset start to plateau. We retain only records with a $\Delta f \geq 10$ Hz (Van Houtte *et al.*, 2014; Ktenidou *et al.*, 2016) and stations that retain the minimum of eight records.

Using our previously described algorithm, we find robust estimation of f_e and f_x in solving for κ on the individual records. Earthquake spectra are complex, and the mathematical forms used to describe them (such as the first derivative) do not always match the ideal functions. Thus, the algorithm sometimes overestimates f_x for certain records. However, we still find the linear fit to model the shape of the decay reasonably well. The use of a weighted regression to solve for κ_0, explained in the next section, also reduces bias from outlier record κ's resulting from a poor frequency determination.

Kappa regression. In the model for high-frequency decay (equation 1), κ represents total high-frequency attenuation, which means it is characterized by local site attenuation as well as attenuation influenced by the wavefield paths. Anderson (1991) formed a model to represent both contributions to κ:

$$\kappa(R, S) = \kappa_0(S) + \tilde{\kappa}(R), \tag{4}$$

in which κ_0 describes attenuation from the shallow subsurface at the site, and $\tilde{\kappa}(R)$ describes attenuation from the path, and is a function of the rupture distance and the overall path attenuation modeled as quality factor Q. To isolate κ_0, we plot the individual records' κ as a function of epicentral distance (Ktenidou *et al.*, 2013) for each station and perform a weighted regression, which considers the uncertainty of the κ estimates (Fig. 3b). This allows us to extrapolate κ at $R_{\text{epi}} = 0$ km, which we accept as κ_0. This method of using Anderson and Hough (1984) to estimate κ for each record at a station and then extrapolating for κ_0 is referred to as the κ_{0_AS} (acceleration spectrum) method in Ktenidou *et al.* (2014). We perform this regression and obtain a κ_0 estimate for each site (Fig. 4a). The uncertainty in κ_0 estimates is obtained from each regression covariance matrix, which is weighted by the individual record κ's and is a propagation of the individual spectra uncertainties.

RESULTS

Site-kappa estimates

We find κ_0 to vary substantially in the SFBA with reliable estimates for ~89% of the stations in our dataset. However, 24 of the stations presented unreliable estimates of κ_0, either due to a negative correlation of κ with distance, a negative κ_0, or obvious site response in the frequency range of interest. A negative correlation contradicts the theoretical understanding that κ (i.e., attenuation) increases with ray-path distance traveled. The negative correlation may be due to a poor polynomial fit, and hence poor frequency range selection or possible bias from unaccounted for site amplification. A negative κ_0 was observed at one station J003, but this is also physically unrealistic as it suggests negative attenuation. We have removed the stations from further analysis, and the following results and figures do not include these stations. However, figures with spectra and their linear fits, as well as R_{epi}–κ regression plots, can be found for all stations online in the Zenodo dataset (Nye *et al.*, 2022b). For a full list of the stations removed, see Table S1.

For the remaining 204 stations, κ_0 estimates range over an order of magnitude from 0.003 to 0.072 s (Fig. 4a), and standard deviations range from 0.002 to 0.028 s (Fig. 4b). Although the spread in values is large, the interquartile range of κ_0 falls between 0.028 and 0.045 s (Fig. 4a). κ_0 exhibits some spatial dependence in the SFBA, which was not imposed a priori and is likely a result of the heterogenous geology of the Bay Area. With this spatial trend, we identify four characteristic zones in the region.

The first (zone 1) is a pocket of larger κ_0 estimates north of the bay around the Santa Rosa plain (SRP) and Rodgers Creek fault (RCF), and extending west to the San Andreas fault (SAF). κ_0 in this zone is moderately high with 80% of the values falling within 0.036–0.046 s. The three stations in zone 1 with the largest κ_0 are MCCM, NSP, and 1835 (0.072, 0.049, 0.049 s, respectively). The generally larger κ_0 in this region likely correlates with the weak, lower velocity material in the plain and basin areas (Sweetkind *et al.*, 2010; Eberhart-Phillips, 2016), as well as possible deformation associated with the SAF.

The second (zone 2) includes the East Bay and the Sacramento–San Joaquin Delta (SSD). This zone also contains moderately large κ_0 values, with 80% of the values falling within 0.034–0.053 s. The three largest estimates in zone 2 are observed at stations 1843, CUSLD, and CBP (all with an estimate of 0.060 s). The larger κ_0 values imply greater attenuation at the stations, which may be consistent with softer material at these sites, including east bay mud and SSD sediments (Hough, 1990; Eberhart-Phillips *et al.*, 2014; Erdem *et al.*, 2019). The abundance of fault zones in the east bay region likely also increases attenuation, as higher fracture density is often associated with lower Q (Eberhart-Phillips, 2014; Eberhart-Phillips, 2016).

The third (zone 3) includes the region around the portion of the SAF extending farther to the south of the bay, near Loma Prieta. Zone 3 includes the largest percentage of higher κ_0 estimates, with 80% of values falling within 0.037–0.052 s. The three largest estimates in this zone are observed at stations SAO, HBH, and HCBB (0.065, 0.059, 0.057 s, respectively). This region contains an abundance of quaternary sediments and weaker rock (Lees and Lindley, 1994), as well as multiple fractured fault zones (the Zayante-Vergeles, San Andreas, and Sargent fault zones).

The fourth and final zone of interest (zone 4) surrounds the SAF along the western side of the bay. The κ_0 estimates at stations near and along this fault are lower than all surrounding regions, with 80% falling within 0.020–0.034 s. The three smallest estimates are observed at stations J045, 1778, and JBG (0.004, 0.005, and 0.005 s, respectively), implying significantly less attenuation. This may be attributed to generally higher-velocity material and harder rock sites (Eberhart-Phillips, 2016).

Producing a regional kappa map

Often, hazards studies require evaluating expected ground motion in regions lacking seismic instrumentation. The hazards

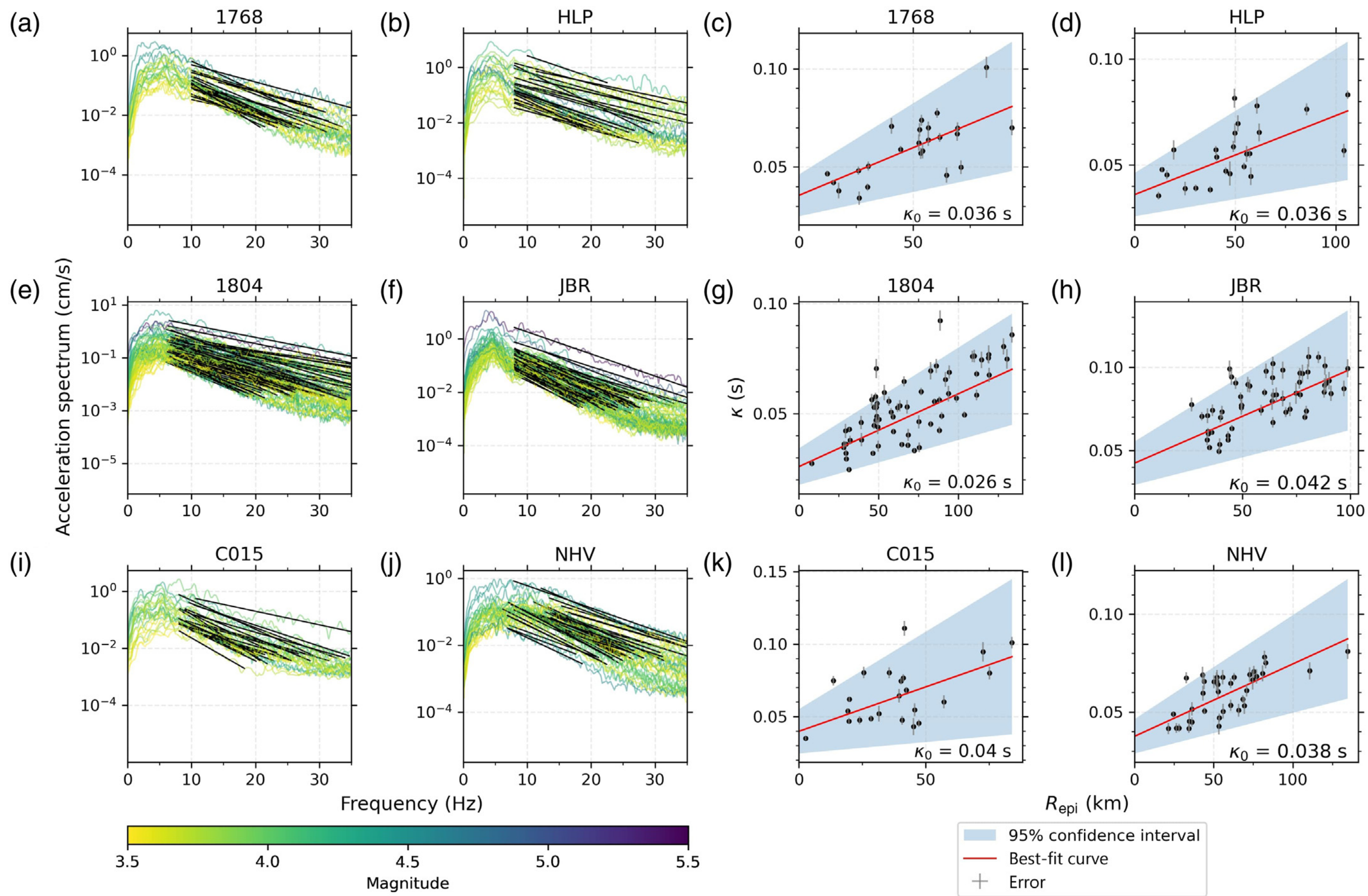

Figure 3. Example station spectra and kappa estimates. (a,b,e,f,i,j) Acceleration spectra recorded at stations 1786, HLP, 1804, JBR, C015, and NHV colored by magnitude. Solid black lines represent the linear fit on each record using the selected frequency ranges. Amplitudes plateau around ~20–30 Hz at stations C015 and JBR demonstrating the effectiveness of our algorithm to avoid such frequency ranges when solving for κ. (c,d,g,h,k,l) Regression of record κ as a function of epicentral distance (R_{epi}) for stations 1786, HLP, 1804, JBR, C015, and NHV. Error bars are indicated by light gray lines, and the 95% confidence interval is represented by the shaded region. κ_0 at stations 1768, HLP, 1804, JBR, C015, and NHV is 0.036, 0.036, 0.026, 0.042, 0.040, and 0.038 s, respectively. The color version of this figure is available only in the electronic edition.

community is also transitioning toward nonergodic GMMs, which require the availability of spatially varying parameters, including a continuous map of κ_0. We use the method of ordinary kriging (OK) to produce a spatially continuous map of κ_0 for the SFBA (Van Houtte *et al.*, 2018) (Fig. 5a). Kriging is a spatial interpolation method that seeks to minimize the prediction error (in our case the prediction of κ_0), and OK assumes a constant mean and variance across the region. Kriging is preferred over simpler spatial-interpolation methods, such as inverse distance weighted interpolation, linear regression, or Gaussian decays, as it assumes a spatial correlation among the data points. It also produces prediction uncertainties, which are often desirable in hazard estimates.

Semivariogram. The first step in spatial interpolation via kriging involves computing a semivariogram of the data. This is a visual representation of how spatially "related" or dependent the data are, and on what spatial scales they correlate (Fig. 5a). The x axis of a semivariogram is the distance between points, and the y axis is the semivariance. The semivariogram typically increases before eventually plateauing, representing data that are no longer correlated. The x and y values at which the semivariogram plateaus are the range and sill, respectively, and the y-intercept is the nugget. The nugget variance (τ^2) represents the spatial variation at distances less than the interstation distances of the dataset or, in other words, near-site randomness. The structure of the computed semivariogram is used to determine the weights of the nearby datapoints in the kriging prediction. Van Houtte *et al.* (2018) assume a semivariogram model with a Matérn order, but we find that a spherical model better fits our data (Fig. 5b). We also compute the semivariogram directly on the κ_0 estimates, whereas Van Houtte *et al.* (2018) assumed a lognormal distribution.

Spatial interpolation. Using the semivariogram covariance model, we interpolate regional κ_0 from the site κ_0 estimates. The resolution of the kriged model is highly dependent on

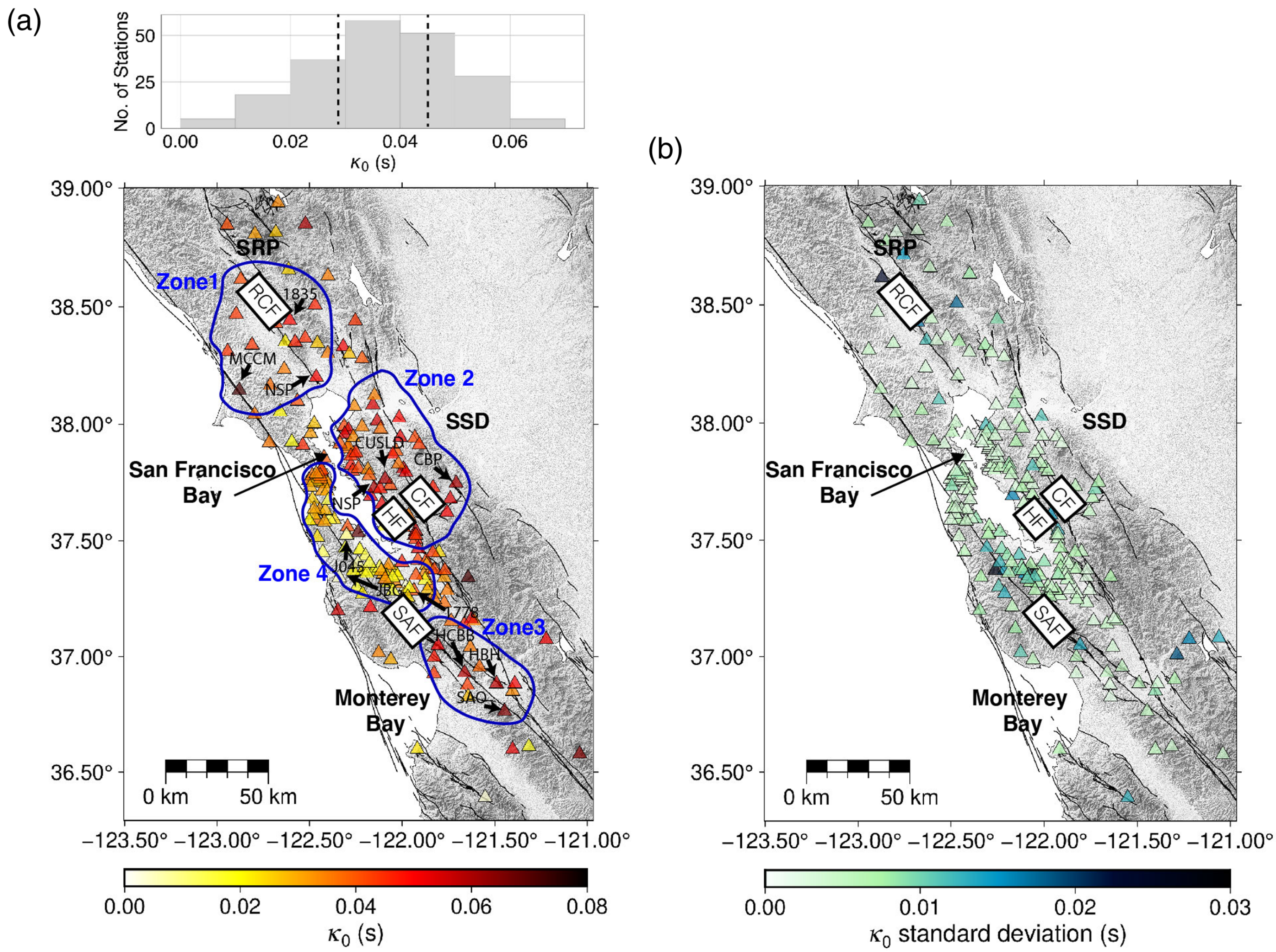

Figure 4. (a) Station-based κ_0 estimates and (b) corresponding standard deviations in our study region. κ_0 estimates range from 0.003 to 0.072 s but most fall between 0.028 and 0.045 s, as indicated by the histogram in (a), where the dashed black lines indicate the interquartile range. Four key zones are highlighted: zone 1: North Bay, zone 2: East Bay, zone 3: South Bay, and zone 4: West Bay. The Sacramento–San Joaquin Delta (SSD) and Santa Rosa Plain (SRP) are labeled, along with the San Andreas fault (SAF), Hayward fault (HF), Calaveras fault (CF), and Rodgers Creek fault (RCF). Other Quaternary faults are also represented by solid black lines. Several key stations mentioned in the Site-kappa estimates section are indicated by the arrows. Zone 1 has κ_0 estimates ranging from 0.021 to 0.072 s, zone 2 has κ_0 estimates ranging from 0.016 to 0.060 s, zone 3 has κ_0 estimates ranging from 0.028 to 0.065 s, and zone 4 has the smallest estimates ranging from 0.004 to 0.069 s. The color version of this figure is available only in the electronic edition.

station density, thus regions with high station density can capture more fine-scale variations in κ_0 with a lower variance than regions with low station density. We cut our model to only retain regions with a variance less than the sill of the semivariogram (1.95×10^{-4} s^2 or 0.014 s), which represents the variance at which the stations are no longer correlated (Fig. 6a). We recommend using this model and refer to it as our "preferred model;" however, we include the full regional model in the supplemental material (see Fig. S2). Both the refined-model and full-model κ_0 predictions range from 0.013 to 0.061 s, and we observe the same general spatial trend as we see with the initial κ_0 estimates, in which κ_0 is the largest to the north, east, and south of the bay and lowest west of the bay. We observe a fine-scale resolution in the κ_0 estimates, especially near the San Francisco Bay where station density is the highest. With this resolution, we observe several pockets of higher κ_0, such as the coastline to the north of Monterey Bay, the northern part of the Calaveras fault (CF), the northern part of the SAF, and the region where the Hayward fault (HF) and CF join in the south. We also observe lower κ_0 zones, such as to the far north of the bay and along the peninsula of the San Francisco Bay. For a comparison of estimated versus predicted κ_0, see Figure S3.

The prediction standard deviations are obtained by taking the square root of the model variance. The standard deviations in our refined-model range from 0.008 to 0.014 s (Fig. 6b). The standard deviation is generally lower for which we have many stations and smoothly increases where station density is sparser. The full and cut .grd files for the kriged κ_0 and standard deviations are accessible on the online Zenodo dataset (Nye *et al.*, 2022b).

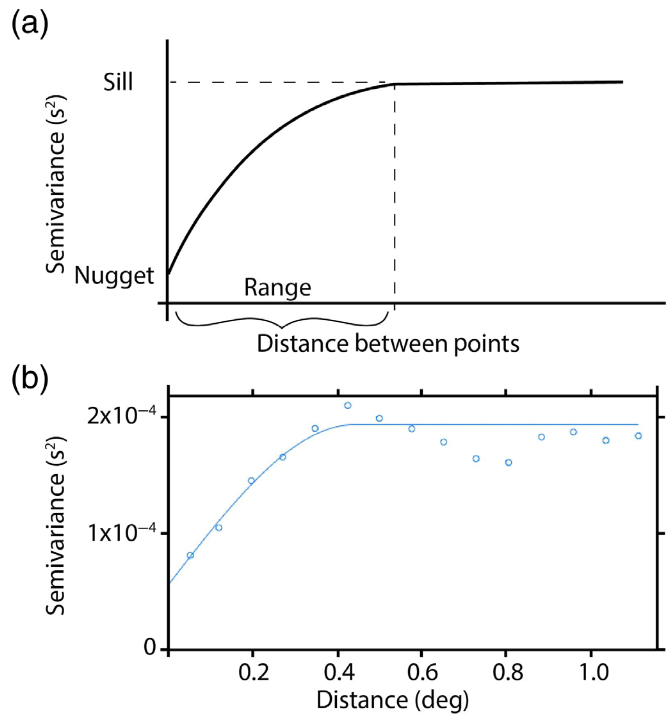

Figure 5. (a) Example semivariogram with the range, sill, and nugget indicated. (b) Binned empirical semivariogram computed for the κ_0 estimates, assuming a spherical model. The oscillation of semivariance past the range could be due to significant variations in geology at moderate distances (such as boundaries between the four highlighted zones in the Site-kappa estimates section). The color version of this figure is available only in the electronic edition.

Site parameter evaluation

One of the main motivations for understanding regional attenuating properties, such as κ_0, is its applicability in GMMs. Most modern GMMs use V_{S30} to approximate site response. However, as previously mentioned, it is not always the singular best representation for site effects. κ has been used in methods for adjusting GMMs to fit non-host regions (Douglas, 2006; Van Houtte *et al.*, 2011; Biro and Renault, 2012; Al Atik *et al.*, 2014), and it has been directly incorporated as a parameter in several modern GMMs (Laurendeau *et al.*, 2013; Hassani and Atkinson, 2018). If shown to consistently be a more suitable site descriptor than or in addition to V_{S30}, κ_0 could be a key component in the development of future GMMs in this region.

GMM implementation. We compare our κ_0 estimates, as well as V_{S30}, with predicted ground motion in the SFBA to evaluate and compare their effectiveness as site parameters in the region. Using the Abrahamson *et al.* (2014; hereafter, ASK14) and Boore *et al.* (2014; hereafter, BA14) GMMs via the OpenQuake engine (Pagani *et al.*, 2014) and the events and sites in our dataset, we compute the predicted intensity measures (IMs), peak ground acceleration (PGA) and peak ground velocity (PGV). ASK14 and BA14 were developed using the Next Generation Attenuation-West2 Project (NGA-West2) dataset (Ancheta *et al.*, 2014) of shallow crustal events, many of which overlap with events in our dataset. We choose the ASK14 and BA14 models as they were regressed on a dataset of events with an **M** > 3, which is suitable for the magnitude range of our events. The inclusion of two GMMs is to further evaluate the relationship of these site parameters with GMMs of varying complexity.

BA14 requires as source parameters the earthquake magnitude, rupture rake, and the depth to the top of rupture (Z_{TOR}), and ASK14 additionally requires the rupture dip and width. Both the models require the closest distance to the rupture plane (R_{RUP}) as the main distance measure as well as the Joyner–Boore distance (R_{JB}), but ASK14 also considers the R_x and R_{y0} distance measures, all of which can be obtained using R_{RUP} and Z_{TOR} (for further explanation of the distance measures, see Abrahamson *et al.*, 2014). Required site parameters include V_{S30} for both the GMMs, and ASK14 additionally requires the depth to the 1 km/s S-wave isosurface ($Z_{1.0}$).

We approximate Z_{TOR} for our small, likely point source, earthquakes as the hypocentral depth, and due to the short source-to-site distances of the records in our dataset, we approximate R_{hyp} as R_{RUP}. To obtain the rupture rake and dip, we follow a hierarchy of sources. We first reference the NGA-West2 finite-fault file (Pacific Earthquake Engineering Research Center, 2013; Ancheta *et al.*, 2014). If the catalog does not contain the event, we reference a catalog obtained through libcomcat query (U.S. Geological Survey, 2020a). Finally, if neither of the catalogs contain the event, we use a default rake and dip of 0° and 90°, respectively, representing a pure strike-slip fault. For the rupture width, we follow a similar hierarchy, first referencing the NGA-West2 finite-fault file. If the event is not found in the catalog, we estimate a rupture width using the Wells and Coppersmith (1984) scaling law for events **M** <5, and the Thingbaijam *et al.* (2017) scaling relation for events **M** >5. For V_{S30}, we use the GMM reference V_{S30} (760 m/s for both models), to correlate the site parameters with modeled ground motion without inherent amplification from incorporating site-specific V_{S30} into the models. Finally, for $Z_{1.0}$, we estimate the depth from the USGS 3D velocity model (U.S. Geological Survey, 2018, 2020b).

Correlation with GMM site residuals. We calculate the rotd50 observed PGA and PGV and compare with predicted values using the ASK14 and BA14 GMMs by computing natural log IM residuals: $\delta\mathrm{IM} = \ln \mathrm{observed} - \ln \mathrm{predicted}$. These residuals are a function of various source, path, and site effects that the GMM does not account for. Using a mixed-effects maximum-likelihood model (e.g., Sahakian *et al.*, 2018; Parker *et al.*, 2020), we decompose the residuals into their event and site contributions to isolate the ground-motion variability resulting solely from local site conditions:

$$\ln(\delta\mathrm{IM}) = \delta E_i + \delta S_j + \delta W_{ij}^0, \quad (5)$$

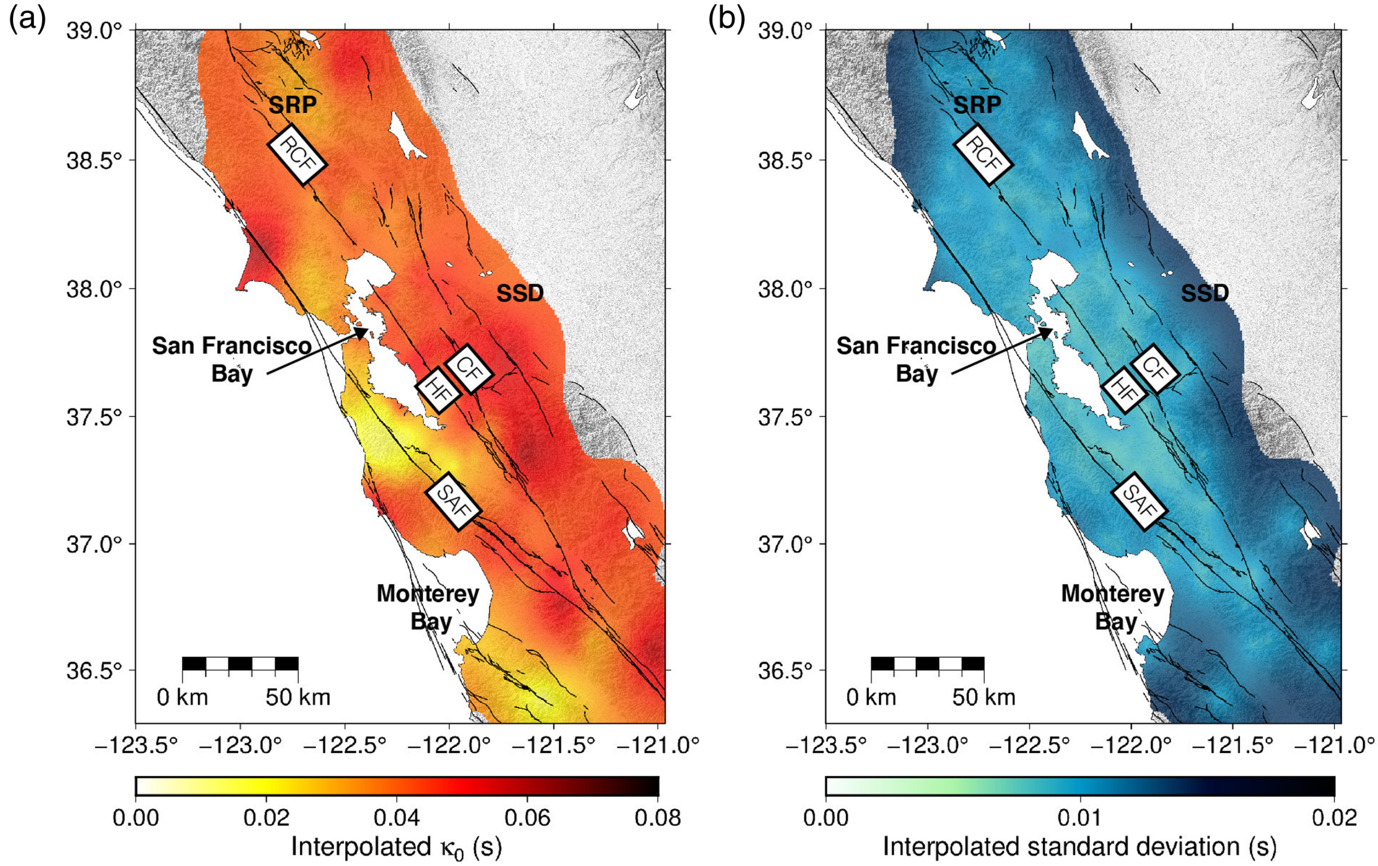

Figure 6. (a) Median interpolated κ_0 for the SFBA and (b) the standard deviation for the kriging predictions. Predictions of κ_0 range from 0.013 s west of the bay to 0.061 s east of the bay. The Sacramento–San Joaquin Delta (SSD) and Santa Rosa Plain (SRP) are labeled, along with the San Andreas fault (SAF), Hayward fault (HF), Calaveras fault (CF), and Rodgers Creek fault (RCF). Other Quaternary faults are also represented by solid black lines. The color version of this figure is available only in the electronic edition.

in which δE_i is the average event mean, δS_j is the site residual, and δW_{ij}^0 represents all other residual components (Baltay *et al.*, 2017; Sahakian *et al.*, 2019).

The site residual δS_j illustrates whether observed ground motion at a site is stronger or weaker than predicted by a GMM due to local geology. For example, a positive site residual for event i at site j would suggest that the observed IM was larger than predicted due to either unaccounted for amplifying effects or less attenuating local conditions. Similarly, a negative site residual would suggest that the observed IM was lower than predicted due to greater regional and local attenuation. We correlate our estimated κ_0 values and V_{S30} with the GMM site residuals to assess the robustness of these parameters to describe ground motion in the SFBA (Fig. 7).

For correlation with the site residuals, we use measured values where available ($V_{S30,\mathrm{meas}}$) and proxy estimates ($V_{S30,\mathrm{proxy}}$) elsewhere. The hierarchy for V_{S30} follows as: measurements from McPhillips *et al.* (2020), measurements and estimates from the NGA-West2 site database file (Pacific Earthquake Engineering Research Center, 2013; Ancheta *et al.*, 2014), and finally estimates from the USGS hybrid global V_{S30} database (Thompson *et al.*, 2014; Heath *et al.*, 2020), with the exception of station GDXB. Although a measured value exists in McPhillips *et al.* (2020), it is unusually high (~1200 m/s) and biases the regressions, so we instead use a proxy value from the NGA-West2 database. Measurements from McPhillips *et al.* (2020) were obtained from a variety of downhole and array-based methods. The NGA-West2 site database uses a combination of geology, geotechnical, geomorphology, and slope-based methods for V_{S30} estimates (Ancheta *et al.*, 2014; Seyhan and Stewart, 2014). The USGS global database uses a slope-based approach to approximate V_{S30} but includes more detailed high-resolution regional maps where available.

We compute simple linear regression between each PGA and PGV site residuals (hereafter referred to as $\delta S_{j,\mathrm{PGA}}$ and $\delta S_{j,\mathrm{PGV}}$, respectively) and the site parameters κ_0 and V_{S30} (Fig. 7). We observe a weak negative correlation between κ_0 and $\delta S_{j,\mathrm{PGA}}$, which indicates that larger values of κ_0 typically result in weaker ground motion than predicted by the GMM (Fig. 7a). This relationship is consistent with our understanding that larger κ_0 describes a site that attenuates high-frequency energy more strongly than other sites. To quantify the statistical significance of the correlation, we examine the Pearson R value, the p-value,

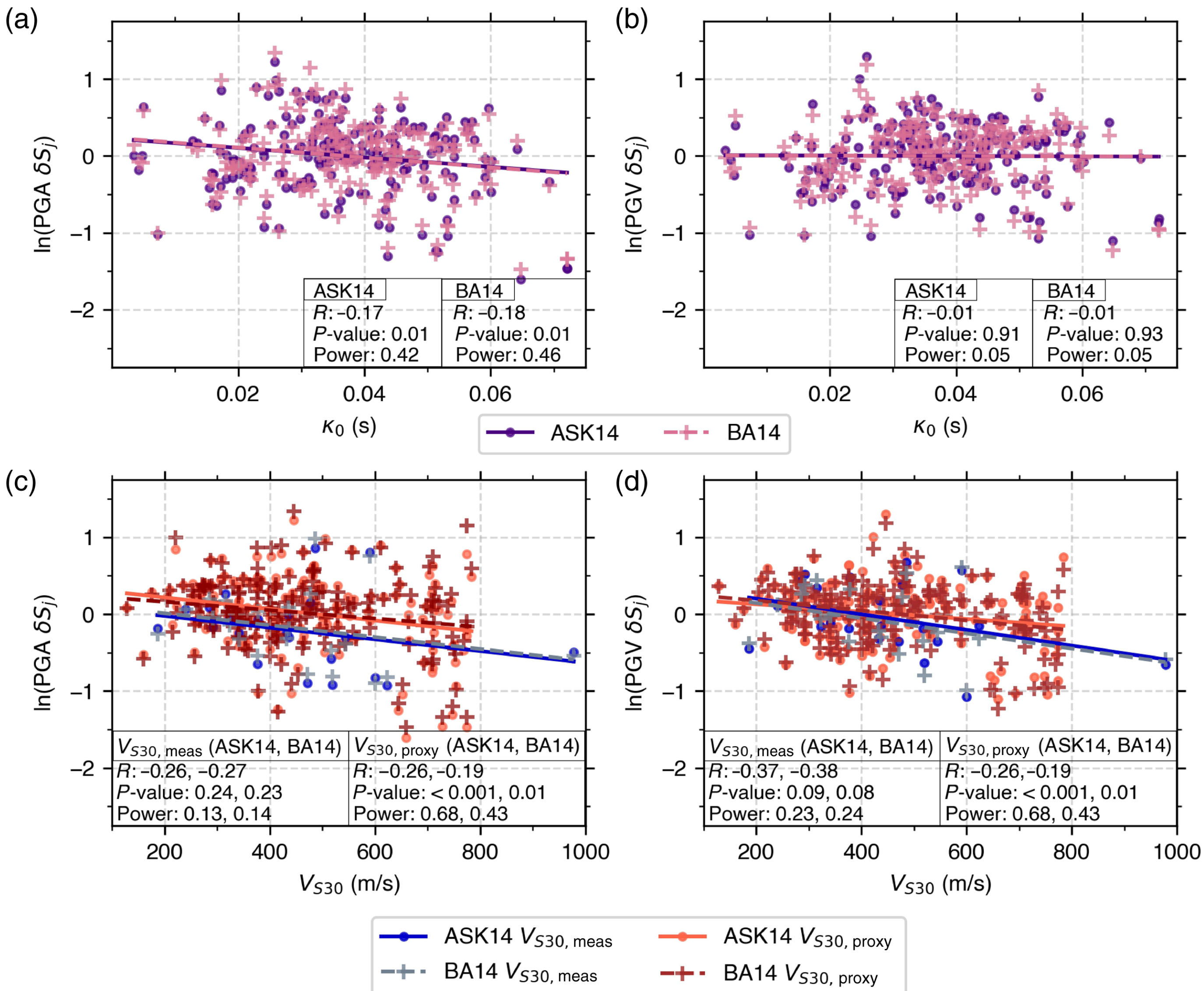

Figure 7. Site parameters κ_0 and V_{S30} versus ground-motion model (GMM) site residuals obtained using the Abrahamson *et al.* (2014; referred as ASK14) and Boore *et al.* (2014; referred as BA14) GMMs. The statistical parameters Pearson-R correlation coefficient (R), p-value, and statistical power (Power) are also indicated. (a) κ_0–$\delta S_{j,\mathrm{PGA}}$ relation shows a weak negative correlation, a statistically significant p-value (<0.05), and a moderate statistical power for both the ASK14 and BA14 GMMs. (b) κ_0–$\delta S_{j,\mathrm{PGV}}$ relation shows a weak, essentially nonexistent correlation, a large p-value, and a low statistical power for both the GMMs. (c) $V_{S30,\mathrm{meas}}$–$\delta S_{j,\mathrm{PGA}}$ and $V_{S30,\mathrm{proxy}}$–$\delta S_{j,\mathrm{PGA}}$ relations show a weak negative correlation for both GMMs. However, correlation with $\delta S_{j,\mathrm{PGA}}$ computed using ASK14 exhibits a more statistically significant relationship compared to BA14 for $V_{S30,\mathrm{proxy}}$. (d) $V_{S30,\mathrm{meas}}$–$\delta S_{j,\mathrm{PGV}}$ and $V_{S30,\mathrm{proxy}}$–$\delta S_{j,\mathrm{PGV}}$ relations also show a weak negative correlation. However $V_{S30,\mathrm{proxy}}$–$\delta S_{j,\mathrm{PGV}}$ is more statistically robust than $V_{S30,\mathrm{meas}}$–$\delta S_{j,\mathrm{PGV}}$, having a low p-value and moderate statistical power for both GMMs. The color version of this figure is available only in the electronic edition.

and the statistical power of the regression. The ASK14 and BA14 κ_0–$\delta S_{j,\mathrm{PGA}}$ regressions have a Pearson R of −0.17 and −0.18, respectively, indicating a weak correlation with reasonable scatter. However, because the p-value is low (<0.05), there is a less than 5% chance that the correlation observed is fictional and influenced by the sample of data. This correlation also has moderate (but not statistically significant, >0.8) statistical powers of 0.42 and 0.46, which indicate an approximate 40% chance that a low p-value (<0.05) will still be observed using a subsample of the data. With all of these factors considered, the κ_0–$\delta S_{j,\mathrm{PGA}}$ correlation is significant, implying that κ_0 is a reasonable predictor of high frequency in our small magnitude dataset.

We second examine the relationship between κ_0 and the PGV site residual ($\delta S_{j,\mathrm{PGV}}$; Fig. 7b). We observe no correlation of κ_0 with $\delta S_{j,\mathrm{PGV}}$, having a Pearson R of −0.01 for both ASK14 and BA14, respectively. The p-value is higher as well (0.91 and 0.93 for ASK14 and BA14, respectively), and we observe a low statistical power (0.05 for both GMMs), suggesting essentially no relationship between κ_0 and PGV.

For V_{S30}, we compare both $V_{S30,\mathrm{meas}}$ and $V_{S30,\mathrm{proxy}}$ with ASK14 and BA14 PGA site residuals individually (Fig. 7c). As with κ_0, we observe a weakly negative correlation with

$\delta S_{j,\mathrm{PGA}}$. This suggests that regions with lower V_{S30} tend to result in higher ground accelerations. $V_{S30,\mathrm{meas}}$–$\delta S_{j,\mathrm{PGA}}$ has a Pearson R of −0.26 and −0.27 for ASK14 and BA14, respectively, whereas $V_{S30,\mathrm{proxy}}$–$\delta S_{j,\mathrm{PGA}}$ has a Pearson R of −0.26 and −0.19. Neither the p-values nor the statistical powers for $V_{S30,\mathrm{meas}}$–$\delta S_{j,\mathrm{PGA}}$ are statistically significant for $V_{S30,\mathrm{meas}}$–$\delta S_{j,\mathrm{PGA}}$. However, the correlation is stronger for $V_{S30,\mathrm{proxy}}$–$\delta S_{j,\mathrm{PGA}}$, especially when considering the ASK14 GMM. The p-value and statistical powers are <0.001 and 0.68, respectively, for ASK14, and 0.01 and 0.43, respectively, for BA14.

We finally compare $V_{S30,\mathrm{meas}}$ and $V_{S30,\mathrm{proxy}}$ with PGV site residuals (Fig. 7d). Again, we observe a weakly negative correlation. $V_{S30,\mathrm{meas}}$ has a stronger correlation with $\delta S_{j,\mathrm{PGV}}$ than with $\delta S_{j,\mathrm{PGA}}$. Here, the Pearson R is the highest for all correlations at −0.37 and −0.39 for ASK14 and BA14, respectively. The p-values are near the statistically significant threshold at 0.09 and 0.07 for ASK14 and BA14, respectively. However, the statistical powers are still low at 0.23 and 0.24. $V_{S30,\mathrm{proxy}}$ exhibits the same level of correlation with $\delta S_{j,\mathrm{PGV}}$ as it does with $\delta S_{j,\mathrm{PGA}}$.

κ_0–V_{S30} relation. As determined in the previous section, κ_0 exhibits the expected correlation with observed ground motion, which supports the motivation of this study to broaden the community κ_0 dataset for seismic hazard applications. Because κ_0 is an observational parameter, seismic recordings are necessary to constrain such values, yet some regions are lacking adequate seismic instrumentation or activity. V_{S30} datasets are more abundant, so a κ_0–V_{S30} relation would prove useful in such circumstances in which κ_0 is required but unavailable. The previous studies have been varied in their conclusions of a κ_0–V_{S30} relation (Silva *et al.*, 1998; Chandler *et al.*, 2006; Drouet *et al.*, 2010; Edwards *et al.*, 2011; Van Houtte *et al.*, 2011; Ktenidou and Van Houtte, 2012; Ktenidou *et al.*, 2012, 2013, 2014, 2015; Klimasewski *et al.*, 2019). Most studies show a negative correlation between the parameters, but the regression models are variable with reasonable scatter. The correlations seem to be influenced, in part, by the study region and inversion method (Ktenidou *et al.*, 2014). One such study in Southern California (Klimasewski *et al.*, 2019) noticed a discrepancy dependent on the method of obtaining V_{S30}, in which measured V_{S30} demonstrated a negative correlation, and proxy V_{S30} demonstrated a very weak positive correlation. We investigate the nature of a relationship between κ_0 and V_{S30} for the SFBA—the only current study of this kind for the region (Fig. 8).

We compare κ_0 with both $V_{S30,\mathrm{meas}}$ where available and $V_{S30,\mathrm{proxy}}$ elsewhere (Fig. 8). The correlation is presented in linear space, but as some V_{S30}–κ_0 correlations have been presented in log–log space (Drouet *et al.*, 2010; Van Houtte *et al.*, 2011; Ktenidou and Van Houtte, 2012; Ktenidou *et al.*, 2012, 2014, 2015), we include a log–log correlation in the supplemental material (see Fig. S4). Other studies provide little justification for the choice of correlation scaling, but we assume a linear relation, and the statistical parameters are not significant for either assumption. As with Klimasewski *et al.* (2019), we observe a weakly negative correlation for $V_{S30,\mathrm{meas}}$–κ_0 and a weakly positive correlation for $V_{S30,\mathrm{proxy}}$–κ_0. However, neither could be considered statistically significant, with both having a large p-value and low statistical power. The κ_0–$V_{S30,\mathrm{meas}}$ and κ_0–$V_{S30,\mathrm{proxy}}$ correlations have a Pearson R of −0.02 and 0.07, a p-value of 0.92 and 0.38, and a statistical power of 0.05 and 0.01, respectively. We expect SFBA sites with larger V_{S30} values (≥ approximately 500 m/s, National Earthquake Hazards Reduction Program [NEHRP] classes B/C; Holzer *et al.*, 2005), such as soft-to-hard rock, to generally be less attenuating, and we find that they are correlated with smaller values of κ_0. Similarly, we expect lower V_{S30} sites (≤ approximately 500 m/s, NEHRP classes C/D; Holzer *et al.*, 2005), such as softer rock or loose sediment, to be more attenuating and correlate with larger values of κ_0. We observe this trend with $V_{S30,\mathrm{meas}}$, but the paucity of measured values likely contributes to the poor correlation.

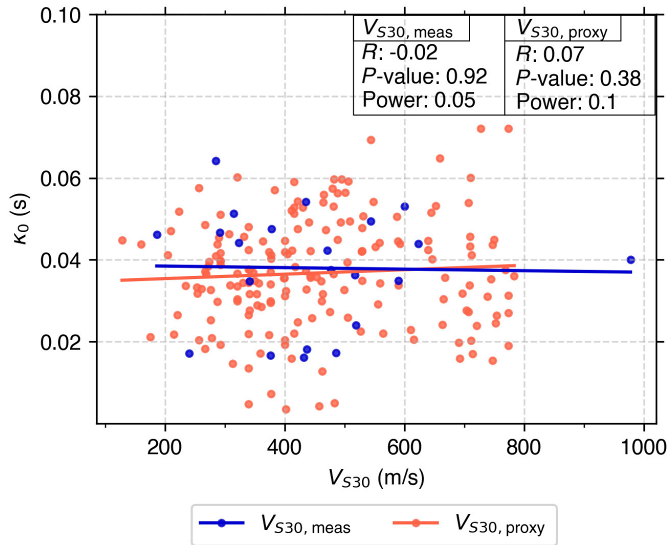

Figure 8. Correlation between κ_0 estimates from this study and both measured and proxy V_{S30} ($V_{S30,\mathrm{meas}}$ and $V_{S30,\mathrm{proxy}}$, respectively). The statistical parameters Pearson-R correlation coefficient (R), p-value, and statistical power (Power) are also indicated. There is a weak, slightly positive correlation between κ_0 and $V_{S30,\mathrm{proxy}}$ and essentially no correlation with $V_{S30,\mathrm{meas}}$. Both the κ_0–$V_{S30,\mathrm{meas}}$ and κ_0–$V_{S30,\mathrm{proxy}}$ relations show no statistical significance with p-values ≫ 0.05 and statistical powers ≪ 0.8. The color version of this figure is available only in the electronic edition.

DISCUSSION

Kappa distance dependence

Most studies of κ have determined a distance dependence, because it is related to the Q-profile and generally increases with epicentral distance. However, the relationships between

κ and distance from such studies are varied. Often, the relationship is assumed to be monotonically linear (Anderson and Hough, 1984; Ktenidou *et al.*, 2013), but some studies have found the relationship to be nonlinear (Anderson, 1991) or varying with distance (Kilb *et al.*, 2012). For example, Kilb *et al.* (2012) only observe a linear relationship for distances between 40 and 70 km. For this study, we assume a linear distance dependence in the regression for κ_0, which we find consistent with our κ versus distance plots. We still observe a linear relationship, even though many of the stations in our dataset recorded events outside of the 40–70 km range (see κ vs. distance plots in the online Zenodo dataset, Nye *et al.*, 2022b).

Relationship between κ_0 and geology

The κ_0 estimates from this study suggest a spatial dependence in the region. We qualitatively investigate the relationships between κ_0 and local geology to evaluate whether this trend is influenced by surficial geology and/or proximity to regional faults.

Shallow geology. The SRP region (zone 1) is covered by thick units of weak, loosely consolidated rocks, which range in thickness up to several kilometers in some basins, such as the Windsor basin to the north and the Cotati basin to the south (Sweetkind *et al.*, 2010). A marine basin is also observed in zone 3, extending between the Zayante and Sargent fault zones (Lees and Lindley, 1994; Eberhart-Phillips, 2016). Weak and unconsolidated materials, such as the layers of silt, clay, sand, gravel, cobbles, and tuffaceous rocks found in these basins, typically have a lower V_S and Q, which influence intrinsic attenuation of energy (Eberhart-Phillips, 2016). Assuming κ is related only to attenuation, it is mathematically equivalent to the full-path attenuation parameter t^* and is inversely related to V_S and Q (Anderson and Hough, 1984; Fletcher and Boatwright, 2020). Thus, the higher κ_0 observed in these zones is consistent with expected attenuation trends and existing attenuation studies of the region (Lees and Lindley, 1994; Eberhart-Phillips, 2016).

Zone 1 also contains volcanic deposits to the southeast of the SRP (U.S. Geological Survey, n.d.). Although these rocks are more compact than the weak basins, they are highly fractured from nearby faults (Sweetkind *et al.*, 2010). Fractures are contributors of high-frequency attenuation, as they scatter energy from higher frequencies to lower frequencies (Frankel, 1991; Kneib and Shapiro, 1992; Abercrombie, 1997). Thus, it makes physical sense that we also estimate moderately high κ_0 values here. This likely also contributes to the larger κ_0 observed near segments of the SAF to the northwest (zone 1) and southeast (zone 3) of the bay, as well as near the HF and CF east of the bay (zone 2). The greater attenuation indicated in these regions is consistent with low-Q zones imaged in the previous attenuation studies of Northern-Central California (Lees and Lindley, 1994; Eberhart-Phillips, 2016).

The east bay region (zone 2) is not only dominated by two major fault zones (HF and CF) and several more minor fault zones, but also mantled by weak material, such as bay mud, artificial fill, and alluvium (Hough, 1990; Eberhart-Phillips, 2016). This zone also encompasses unconsolidated sediments in the SSD, which is sourced from the Sacramento and San Joaquin rivers—two of the largest rivers in California. The thick units of weak material characterizing this region correlate with larger κ_0 from this study as well as low Q from other attenuation studies of the SSD (Eberhart-Phillips *et al.*, 2014; Erdem *et al.*, 2019).

The shoreline along the western edge of the bay (zone 4) stands out as having some of the smallest values of κ_0 in the SFBA. Although zone 4 contains some alluvial units, the peninsula is more widely dominated by uplifted sedimentary, volcanic, and metamorphic rocks of the Franciscan and Great Valley complexes (U.S. Geological Survey, n.d.). The absence of much surficial sediment west of the shoreline likely allows for greater preservation of high-frequency energy. Another consideration for the low κ_0 in this zone is that the SAF could act as a waveguide, thus amplifying high-frequency energy from trapped waves. Evidence of this effect has been observed in southern sections of the fault zone (Li and Teng, 1990; Li *et al.*, 2004; Olsen *et al.*, 2006). However, this effect appears to be localized to the peninsula. Other sections of the SAF exhibit higher values of κ_0 (zones 1 and 3). The greater preservation of high-frequency energy in this region is especially pertinent for seismic hazard, as the SAF is a source of large earthquakes.

Although much of the SFBA exhibits attenuating conditions that could reduce the seismic hazard associated with high-frequency ground motion, this same material can also result in strong amplification of low frequencies if a sharp impendence boundary exists below the sediment layer (Aki, 1988; Hough, 1990; Aki, 1993). As low-frequency amplification can still have a great effect on the resilience of structures enduring earthquake ground motion when considering resonant frequencies of structures, these high κ_0 regions should not be disregarded as regions of seismic hazard or risk.

Fault zones. The SFBA is an active tectonic region and contains several major active faults previously mentioned, including the SAF, HF, CF, and RCF as well as numerous other minor faults. It is well known that fault activity can deform the surrounding wall rock resulting in a fault damage zone characterized by microfractures, folds, and fractured rock (Choi *et al.*, 2016). It is reasonable to assume that such zones would influence seismic attenuation, so we investigate the relationship between κ_0 and proximity to faults.

Determining the boundaries of fault damage zones has varied between studies, resulting in damage zone widths that span orders of magnitude (Choi *et al.*, 2016). In California, studies have determined fault zone widths ranging between tens of meters up to around 1.5 km (e.g., Schulz and Evans, 2000;

Cochran *et al.*, 2009; Powers and Jordan, 2010; Li *et al.*, 2016; Ostermeijer *et al.*, 2020). For the sake of simplicity, we assume an average fault zone width of 1 km and evaluate κ_0 of stations located within this boundary for the SAF, HF, CF, and RCF. For a more detailed analysis of the effect from fault damage zones on κ_0 estimates, one could perform a seismic velocity study to better determine the damage zone boundaries for each fault of interest (e.g., Cochran *et al.*, 2009).

For the previous criteria, we find an average κ_0 of 0.040 s for stations within the damage zones and 0.037 s for stations outside the damage zones. The higher attenuation observed within the fault zones could be due to the fractured, heterogeneous properties of the surrounding rock. We perform a Kolmogorov–Smirnov (K-S) hypothesis test on these datasets to evaluate the significance of the relationship, and we observe a D-statistic of 0.21 and a p-value of 0.31. The low D-statistic (<0.31: critical value for dataset sample size) and the large p-value both suggest that the two datasets are statistically similar, thus suggesting little relationship between κ_0 and fault damage zones. This could be an indication of the scale at which regional geology influences κ_0, but it could also be biased by the few stations within our designated fault zones (22). Increased instrumentation within fault deformation zones has been of recent interest in the geophysical community to better constrain rupture processes and could also provide information for site response within a fault zone. The Community Near-Fault Observatory—a current Incorporated Research Institutions for Seismology instrumentation initiative (IRIS, n.d.) has proposed installing instruments across major faults in Southern California, but a similar initiative in the SFBA could be an avenue for future work.

Comparison with other regional studies

This is the first regional κ_0 study of the SFBA; however, there have been several κ_0 studies in Southern California near the San Jacinto Fault (SJF) zone (Anderson 1991; Kilb *et al.*, 2012; Klimasewski *et al.*, 2019; Johnson *et al.*, 2020). Their estimates ranged from 0.002 to 0.023, 0.021 to 0.037, 0.022 to 0.047, and 0.017 to 0.059 s, respectively. A majority of estimates from this study fall within the range of values from studies in Southern California, but the SFBA exhibits greater high-frequency attenuation as indicated by the larger upper range (0.072 s). Geology around the SJF is more homogenous than in the SFBA, and is characterized more by volcanic and metamorphic and other consolidated rocks, whereas the SFBA contains significantly more loose sedimentary cover. Thus, we find the larger estimates of this study to be in line with the trend of other studies.

κ_0 and V_{S30} as site parameters

Correlation with observed ground motion. Our study is motivated by the assumption that κ_0 is a suitable descriptor of site characteristics, and that seismic hazard studies can benefit from its inclusion as a site parameter. Although it has been studied for several decades, literature on κ is still limited, thus we aim to explore this assumption with our κ_0 estimates to evaluate its robustness. We find a modest correlation between κ_0 with site terms from small to moderate magnitude earthquake PGA in the SFBA; however, significant scatter is observed. Although PGA is generally understood to come from higher frequency ground motion based on theoretical source spectra (Brune, 1970), some studies have found PGA to be influenced by a wider frequency band (Bora *et al.*, 2016; Ktenidou , 2022). Acceleration amplitudes could also be controlled by low-frequency ground motion, if amplification from near-site conditions overpowers high-frequency energy. Considering that the SFBA is dominated by weak sites, this could also be a contributing factor in the scatter. Nevertheless, the trend observed supports our understanding of κ_0, in which PGA site response shows a negative relationship with κ_0. The negative relationship indicates that sites with a larger κ_0 (greater high-frequency attenuation) experience weaker peak ground motion, which is consistent with results from Klimasewski *et al.* (2019). Although κ_0 correlates well with $\delta S_{j,\mathrm{PGA}}$, V_{S30} correlates equally well when considering proxy values. Thus, both could be considered reasonable parameters for PGA studies in the SFBA. However, although one might think to disregard κ_0, considering its equivalent performance to V_{S30}, both provide uniquely important information about the ground motion and frequency content, and, as such, κ_0 would still be a useful parameter in future ground-motion studies of the region. In particular, κ_0 could be a useful parameter for modeling FAS at higher frequencies (e.g., Bayless and Abrahamson, 2018). We did not consider FAS GMM site residuals in this study, but this could be another avenue for future work.

There is essentially no relationship between κ_0 and $\delta S_{j,\mathrm{PGV}}$, as indicated by the κ_0–$\delta S_{j,\mathrm{PGV}}$ results (Fig. 7b), which is unsurprising as PGV is understood to be derived from a lower frequency range than PGA, and κ_0 is considered a high-frequency parameter (Brune, 1970). V_{S30}, whether measured or proxy, would be a more robust site parameter for PGV studies.

These analyses were performed using site residuals obtained from two different GMMs of varying complexity. Relevant to site effects, ASK14 includes $Z_{1.0}$ in addition to V_{S30}, which is also included in BA14. We find that κ_0 relates comparably to site residuals from both the GMMs, suggesting that the addition of $Z_{1.0}$ does not account for high-frequency attenuation. This is unsurprising as $Z_{1.0}$ is included in models to account for basin effects, which is usually an amplification of low-frequency energy. However, V_{S30} relates slightly better with site residuals from the more complex ASK14 GMM. This suggests that the addition of $Z_{1.0}$ accounts for some site effects unaccounted for by V_{S30}. Thus, the remaining site effects after including basin effects a priori are better attributed to V_{S30}.

κ_0–V_{S30} relation. Although V_{S30} has shown to be limited in its application as a proxy for site conditions in some studies, it is often the only site measurement accessible. Because of this, we found it profitable to examine the relationship between V_{S30} and κ_0 for when κ_0 measurements are not available. $V_{S30,\mathrm{meas}}$ correlates negatively with κ_0, which is consistent with most other κ_0–V_{S30} studies (Silva *et al.*, 1998; Chandler *et al.*, 2006; Drouet *et al.*, 2010; Edwards *et al.*, 2011; Van Houtte *et al.*, 2011; Ktenidou and Van Houtte, 2012; Ktenidou *et al.*, 2012, 2013; Klimasewski *et al.*, 2019). Lower V_{S30} units ($\leq \sim 500$ m/s), such as weak rock, soft soil, and loose sediments tend to attenuate high-frequency energy, as V_{S30} and Q are inversely related to intrinsic attenuation (Anderson and Hough, 1984). Neither correlation with $V_{S30,\mathrm{meas}}$ or $V_{S30,\mathrm{proxy}}$ could be considered statistically significant, but $V_{S30,\mathrm{meas}}$ exhibits a stronger correlation with κ_0 than $V_{S30,\mathrm{proxy}}$. If measurements of V_{S30} are available, V_{S30} could be used as a proxy for κ_0, but the use of V_{S30} estimates as a proxy would likely result in more unreliable estimates of κ_0.

CONCLUSIONS

In this study, we estimate the high-frequency attenuation parameter κ_0 for 228 stations in the SFBA following the method of Anderson and Hough (1984). Our results show a range in values from 0.003 to 0.072 s, with most falling between 0.028 and 0.045 s. The spatial distribution of κ_0 suggests a spatial dependence that is controlled, in part, by the heterogeneous shallow geology of the region. The largest κ_0 estimates are observed to the north, east, and south of the bay, especially in the SSD, whereas the smallest are observed on the western peninsula around the SAF.

We further evaluate κ_0 as a site parameter and compare it with the commonly used V_{S30}. κ_0 correlates well with PGA, which is promising for future seismic hazard applications. Correlations of ground motion with V_{S30} can be equally reliable but are sensitive to whether V_{S30} is measured or obtained by proxy. Interestingly, proxy values for V_{S30} correlate better with PGA, but this could be biased by the limited V_{S30} measurements.

The regional map of κ_0 from this study may be a useful contribution to future hazard studies in the SFBA. Ideally, κ_0 would be incorporated directly as a site parameter in the development of new GMMs, especially in regions where sufficient data exist to develop fine-resolution models. Even if the development of new GMMs is unlikely in the foreseeable future, these models are still valuable in host-to-site adjustments that have typically used an average value of κ to describe the entire region. Site-specific κ adjustments would better constrain expected ground motion and hazards, especially in regions with fine-scale heterogeneities in regional geology.

It is important to recognize that the results presented in this study are based on weaker ground motions. The relationship between κ_0 and soil response resulting from stronger ground motions has been investigated in several studies (Ktenidou *et al.*, 2015; Ji *et al.*, 2021), and a moderate correlation has been observed where stronger ground motion results in smaller κ_0. However, the magnitude of the effects of soil nonlinearity is site dependent, and it seems to be a greater factor with softer sites (Ji *et al.*, 2021). As the SFBA is dominated mostly by softer shallow geologic conditions and has the possibility of experiencing shaking from **M**∼8 events, these effects are important to consider in ground-motion studies of the SFBA.

We also recognize the limitations of κ_0 in that it is solely a high-frequency parameter and does not account for low-frequency amplification—an important consideration especially in engineering of large structures. Thus, characterization of other site metrics, where available, could contribute important additional information in seismic hazard studies.

DATA AND RESOURCES

Our earthquake catalog was accessed from the U.S. Geological Survey (USGS) on August 2019 using ObsPy (Beyreuther *et al.*, 2010). Broadband and strong-motion seismic records were downloaded from the Northern California Earthquake Data Center (NCEDC) using ObsPy (last accessed June 2022). Seismic records belong to the BK (Northern California Earthquake Data Center, 2014), BG (no doi), NC (USGS Menlo Park, 1967), NP (U.S. Geological Survey, 1931), and WR (no doi) seismic networks. Fault geometries were obtained through the USGS Fault and Fold database (U.S. Geological Survey, 2017, last accessed August 2017). Measured V_{S30} values were taken from the McPhillips *et al.* (2020) catalog. Estimated V_{S30} values were downloaded from the Next Generation Attenuation-West2 Project (NGA-West2) site database file (Pacific Earthquake Engineering Research Center, 2013; Ancheta *et al.*, 2014) and USGS hybrid global V_{S30} database (Thompson *et al.*, 2014; Heath *et al.*, 2020). The global database was last accessed on August 2021. The USGS 3D velocity model of the Bay Area was queried using CenCalVM (U.S. Geological Survey, 2018, 2020b). Maps were produced using the Generic Mapping Tools (GMT) software (Wessel *et al.*, 2019) with a digital elevation model downloaded from GMTSAR (Sandwell *et al.*, 2011), and all the analyses were completed with in-house code, available online at https://github.com/taranye96/kappa_bayarea (last accessed November 2022). This includes the code to determine f_e and f_x, compute κ on individual spectra, complete the regressions, and spatially interpolate κ_0. The supplemental material contains figures showing example station earthquake-based horizontal-to-vertical spectral ratio (eHVSR) plots, a regional kappa map for the entire SFBA, a scatterplot of estimated versus interpolated κ_0, a log–log V_{S30}–κ_0 plot, and a table listing stations with less reliable estimates of κ_0. Other supporting material can be found in the Zenodo dataset (Nye *et al.*, 2022b), which includes the eHVSR curves, spectra, and κ_0 regression plots for each station, .kml and .txt files of the κ_0 estimates, and .grd files of the kriged κ_0 predictions. Initial efforts for this project using different methodology were presented at the 2019 Southern California Earthquake Center (SCEC) Annual Meeting (King *et al.*, 2019). Preliminary data processing and station κ_0 results using the updated methodology were presented at the 2022 12th National Conference on Earthquake Engineering (Nye *et al.*, 2022a), but results differ slightly in this paper due to corrections in data processing and minor revisions to methodology.

DECLARATION OF COMPETING INTERESTS

The authors acknowledge that there are no conflicts of interest recorded.

ACKNOWLEDGMENTS

The authors are grateful to the U.S. Geological Survey (USGS) for supporting this work under the USGS EHP Grant Number G19AP00071. The authors graciously thank Susan Hough as a USGS internal reviewer, as well as Samantha Palmer and a second anonymous reviewer, whose comments and revisions enhanced the quality and scientific rigor of this article. The authors also give special thanks to Stefano Parolai and Ashly Cabas for providing their valuable insight on the relationships between site response and κ.

Any use of trade, firm, or product names is for descriptive purposes only and does not imply endorsement by the U.S. Government.

REFERENCES

Aagaard, B. T., and E. T. Hirakawa (2021). San Francisco Bay region 3D seismic velocity model v21.1, *U.S. Geol. Surv. Data Release* [Data Set], doi: 10.5066/P9TRDCHE.

Abercrombie, R. E. (1997). Near-surface attenuation and site effects from comparison of surface and deep borehole recordings, *Bull. Seismol. Soc. Am.* **87,** no. 3, 731–744, doi: 10.1785/BSSA0870030731.

Abrahamson, N. A., W. J. Silva, and R. Kamai (2014). Summary of the ASK14 ground motion relation for active crustal regions, *Earthq. Spectra* **30,** no. 3, 1025–1055, doi: 10.1193/070913EQS198M.

Aki, K. (1988). Local site effects on strong ground motion, in *Earthquake Engineering and Soil Dynamics II—Recent Advances in Ground Motion Evaluation*, J. Lawrence Von Thun (Editor), Geotechnical Special Publication 20, Am. Soc. Civil Eng., New York, 103–155.

Aki, K. (1993). Local site effects on weak and strong ground motion, *Tectonophysics* **218,** nos. 1–3, 93–111, doi: 10.1016/0040-1951(93)90262-I.

Al Atik, L., A. Kottke, N. Abrahamson, and J. Hollenback (2014). Kappa (κ) scaling of ground-motion prediction equations using an inverse random vibration theory approach, *Bull. Seismol. Soc. Am.* **104,** no. 1, 336–346, doi: 10.1785/0120120200.

Ancheta, T. D., R. B. Darragh, J. P. Stewart, E. Seyhan, W. J. Silva, B. S.-J. Chiou, K. E. Wooddell, R. W. Graves, A. R. Kottke, D. M. Boore, *et al.* (2014). NGA-West2 database, *Earthq. Spectra* **30,** no. 3, 989–1005, doi: 10.1193/070913EQS197M.

Anderson, J. G. (1986). Implication of attenuation for studies of the earthquake source, in *Earthquake Source Mechanics*, S. Das, J. Boatwright, and C. H. Scholz (Editors), doi: 10.1029/GM037p0311.

Anderson, J. G. (1991). A preliminary descriptive model for the distance dependence of the spectral decay parameter in southern California, *Bull. Seismol. Soc. Am.* **81,** no. 6, 2186–2193, doi: 10.1785/BSSA0810062186.

Anderson, J. G., and S. E. Hough (1984). A model for the shape of the Fourier amplitude spectrum of acceleration at high frequencies, *Bull. Seismol. Soc. Am.* **74,** no. 5, 1969–1993, doi: 10.1785/BSSA0740051969.

Anderson, J., and J. Humphrey (1991). A least squares method for objective determination of earthquake source parameters, *Seismol. Res. Lett.* **62,** nos. 3/4, 201–209, doi: 10.1785/gssrl.62.3-4.201.

Askan, A., F. N. Sisman, and O. Pekcan (2014). A regional near-surface high frequency spectral attenuation (kappa) model for northwestern Turkey, *Soil Dynam. Earthq. Eng.* **65,** 113–125, doi: 10.1016/j.soildyn.2014.06.007.

Atkinson, G. M., and I. Beresnev (1997). Don't call it stress drop, *Seismol. Res. Lett.* **68,** no. 1, 3–4, doi: 10.1785/gssrl.68.1.3.

Baltay, A. S., and T. C. Hanks (2014). Understanding the magnitude dependence of PGA and PGV in NGA-West 2 data, *Bull. Seismol. Soc. Am.* **104,** no. 6, 2851–2865, doi: 10.1785/0120130283.

Baltay, A. S., T. C. Hanks, and N. A. Abrahamson (2017). Uncertainty, variability, and earthquake physics in ground-motion prediction equations, *Bull. Seismol. Soc. Am.* **107,** no. 4, 1754–1772, doi: 10.1785/0120160164.

Bayless, J., and N. A. Abrahamson (2018). An empirical model for Fourier amplitude spectra using the NGA-West2 database, *PEER Rept. 2018/07*, Pacific Earthquake Engineering Research Center, University of California, Berkeley, California.

Beyreuther, M., R. Barsch, L. Krischer, T. Megies, Y. Behr, and J. Wassermann (2010). ObsPy: A Python toolbox for seismology, *Seismol. Res. Lett.* **81,** no. 3, 530–533, doi: 10.1785/gssrl.81.3.530.

Biasi, G., and K. D. Smith (2001). Final Project Report, "Site effects for seismic monitoring stations in the vicinity of Yucca Mountain, Nevada", *Prepared for the US DOE/UCCSN Cooperative Agreement Number DE-FC08-98NV12081, Task 12*, Southern Great Basin Seismic Network Operations (SGBSN), MOL.20011204.0045.

Biro, Y., and P. Renault (2012). Importance and impact of host-to-target conversions for ground motion prediction equations in PSHA, *Proc. of the 15th World Conf. of Earthquake Engineering*, Lisbon, Portugal, 4–28 September.

Boore, D. M. (2003). Simulation of ground motion using the stochastic method, *Pure Appl. Geophys.* **160,** nos. 3/4, 635–676, doi: 10.1007/PL00012553.

Boore, D. M., W. B. Joyner, and T. E. Fumal (1993). Estimation of response spectra and peak accelerations from western North American earthquakes: An interim report, *U.S. Geol. Surv. Open-File Rept. 93-509*, 72 pp.

Boore, D. M., J. P. Stewart, E. Seyhan, and G. Atkinson (2014). NGA-West2 equations for predicting PGA, PGV, and 5% damped PSA for shallow crustal earthquakes, *Earthq. Spectra* **30,** no. 3, 1057–1085, doi: 10.1193/070113EQS184M.

Bora, S. S., F. Scherbaum, N. Kuehn, and P. Stafford (2016). On the relationship between Fourier and response spectra: Implications for the Adjustment of empirical ground-motion prediction equations (GMPEs), *Bull. Seismol. Soc. Am.* **106,** no. 3, 1235–1253, doi: 10.1785/0120150129.

Borcherdt, R. D. (1994). Estimates of site-dependent response spectra for design (methodology and justification), *Earthq. Spectra* **10,** no. 4, 617–653, doi: 10.1193/1.1585791.

Brocher, T., B. Aagaard, R. Simpson, and R. Jachens (2006). The new USGS 3D seismic velocity model of northern California (abstract), *Seismol. Res. Lett.* **77,** no. 124, 271.

Brune, J. N. (1970). Tectonic stress and the spectra of seismic shear waves from earthquakes, *J. Geophys. Res.* **75,** no. 26, 4997–5009, doi: 10.1029/JB075i026p04997.

Campbell, K. W., and Y. Bozorgnia (2008). NGA ground motion model for the geometric mean horizontal component of PGA, PGV, PGD and 5% damped linear elastic response spectra for

periods ranging from 0.01 to 10 s, *Earthq. Spectra* **24,** no. 1, 139–171, doi: 10.1193/1.2857546.
Castro, R. R., and L. L. Ávila-Barrientos (2015). Estimation of the spectral parameter kappa in the region of the Gulf of California, Mexico, *J. Seismol.* **19,** 809–829, doi: 10.1007/s10950-015-9496-x.
Castro, R. R., L. Colavitti, C. A. Vidales-Basurto, F. Pacor, S. Sgobba, and G. Lanzano (2022). Near-source attenuation and spatial variability of the spectral decay parameter kappa in central Italy. *Seismol. Res. Lett.* **93,** no. 4, 2299–2310, doi: 10.1785/0220210276.
Çelebi, M., V. J. Sahakian, D. Melgar, and L. Quintanar (2018). The 19 September 2017 M 7.1 Puebla-Morelos earthquake: Spectral ratios confirm Mexico City Zoning, *Bull. Seismol. Soc. Am.* **108,** no. 6, 3289–3299, doi: 10.1785/0120180100.
Chandler, A. M., N. T. K. Lam, and H. H. Tsang (2006). Near-surface attenuation modelling based on rock shear-wave velocity profile, *Soil Dynam. Earthq. Eng.* **26,** no. 11, 1004–1014, doi: 10.1016/j.soildyn.2006.02.010.
Choi, J. H., P. Edwards, K. Ko, and Y. S. Kim (2016). Definition and classification of fault damage zones: A review and a new methodological approach, *Earth Sci. Rev.* **152,** 70–87, doi: 10.1016/j.earscirev.2015.11.006.
Cochran, E. S., Y. G. Li, P. M. Shearer, S. Barbot, Y. Fialko, and J. E. Vidale (2009). Seismic and geodetic evidence for extensive, long-lived fault damage zones, *Geology* **37,** no. 4, 315–318, doi: 10.1130/G25306A.1.
Dalton, C. A., G. Ekström, and A. M. Dziewonski (2009). Global seismological shear velocity and attenuation: A comparison with experimental observations, *Earth Planet. Sc. Lett.* **284,** nos. 1/2, 65–75, doi: 10.1016/j.epsl.2009.04.009.
Douglas, J. (2006). Ground-motion prediction equations for southern Spain and southern Norway obtained using the composite model perspective, *J. Earthq. Eng.* **10,** no. 1, 33–72, doi: 10.1142/S1363246906002566.
Douglas, J., and B. Edwards (2016). Recent and future developments in earthquake ground motion estimation, *Earth Sci. Rev.* **160,** 203–219, doi: 10.1016/j.earscirev.2016.07.005.
Douglas, J., P. Gehl, L. F. Bonilla, and C. Gélis (2010). A κ model for mainland France, *Pure Appl. Geophys.* **167,** no. 11, 1303–1315, doi: 10.1007/s00024-010-0146-5.
Drouet, S., F. Cotton, and P. Guéguen (2010). VS30, κ, regional attenuation and Mw from accelerograms: Application to magnitude 3–5 French earthquakes, *Geophys. J. Int.* **182,** no. 2, 880–898, doi: 10.1111/j.1365-246X.2010.04626.x.
Eberhart-Phillips, D. (2016). Northern California seismic attenuation: 3D Qp and Qs models, *Bull. Seismol. Soc. Am.* **106,** no. 6, 2558–2573, doi: 10.1785/0120160060.
Eberhart-Phillips, D., C. Thurber, and J. B. Fletcher (2014). Imaging P and S attenuation in the Sacramento–San Joaquin Delta Region, Northern California, *Bull. Seismol. Soc. Am.* **104,** no. 5, 2322–2336, doi: 10.1785/0120130336.
Edwards, B., D. Fäh, and D. Giardini (2011). Attenuation of seismic shear wave energy in Switzerland, *Geophys. J. Int.* **185,** no. 2, 967–984, doi: 10.1111/j.1365-246X.2011.04987.x.
Erdem, J. E., J. Boatwright, and J. B. Fletcher (2019). Ground-motion attenuation in the Sacramento–San Joaquin Delta, California, from 14 Bay Area Earthquakes, including the 2014 M 6.0 South Napa Earthquake, *Bull. Seismol. Soc. Am.* **109,** no. 3, 1025–1033, doi: 10.1785/0120180182.
Fernández, A. I., R. R. Castro, and C. I. Huerta (2010). The spectral decay parameter kappa in northeastern Sonora, Mexico. *Bull. Seismol. Soc. Am.* **100,** no. 1, 196–206, doi: 10.1785/0120090049.
Fletcher, J. B., and J. Boatwright (2020). Peak ground motions and site response at Anza and Imperial Valley, California, *Pure Appl. Geophys.* **177,** 2753–2769, doi: 10.1007/s00024-019-02366-2.
Frankel, A. (1991). Mechanisms of seismic attenuation in the crust: Scattering and anelasticity in New York State, South Africa, and southern California, *J. Geophys. Res.* **96,** no. B4, 6269–6289, doi: 10.1029/91JB00192.
Gordon, R. B., and L. A. Davis (1968). Velocity and attenuation of seismic waves in imperfectly elastic rock, *J. Geophys. Res.* **73,** no. 12, 3917–3935, doi: 10.1029/JB073i012p03917.
Graves, R. W., and A. Pitarka (2004). Broadband time history simulation using a hybrid approach, *Proc. of the 13th World Conf. of Earthquake Engineering*, paper no. 1098, Vancouver, Canada.
Haendel, A., J. G. Anderson, M. Pilz, and F. Cotton (2020). A frequency-dependent model for the shape of the Fourier amplitude spectrum of acceleration at high frequencies, *Bull. Seismol. Soc. Am.* **110,** no. 6, 2742–2754, doi: 10.1785/0120200118.
Hanks, T. C. (1982). Fmax, *Bull. Seismol. Soc. Am.* **72,** no. 6, 1867–1879, doi: 10.1785/BSSA07206A1867.
Hanks, T. C., and H. Kanamori (1979). A moment magnitude scale, *J. Geophys. Res.* **84,** no. B5, 2348–2350, doi: 10.1029/JB084iB05p02348.
Hanks, T. C., and W. Thatcher (1972). A graphical representation of seismic source parameters, *J. Geophys. Res.* **77,** no. 23, 4393–4405, doi: 10.1029/jb077i023p04393.
Hassani, B., and G. M. Atkinson (2018). Adjustable generic ground-motion prediction equation based on equivalent point-source simulations: Accounting for kappa effects, *Bull. Seismol. Soc. Am.* **108,** no. 2, 913–928, doi: 10.1785/0120170333.
Heath, D., D. J. Wald, C. B. Worden, E. M. Thompson, and G. Scmocyk (2020). A global hybrid VS30 map with a topographic-slope-based default and regional map insets, *Earthq. Spectra* **36,** no. 3, 1570–1584, doi: 10.1177/8755293020911137.
Holzer, T. L., A. C. Padovani, M. J. Bennett, T. E. Noce, and J. C. Tinsley (2005). Mapping NEHRP VS30 site classes, *Earthq. Spectra* **21,** no. 2, 353–370, doi: 10.1193/1.1895726.
Hough, S. E. (1990). Constraining sediment thickness in the San Francisco Bay area using observed resonances and P-to-S conversions, *Geophys. Res. Lett.* **17,** no. 9, 1469–1472, doi: 10.1029/GL017i009p01469.
Hough, S. E., and J. G. Anderson (1988). High-frequency spectra observed at Anza, California: Implications for Q structure (USA), *Bull. Seismol. Soc. Am.* **78,** no. 2, 692–707, doi: 10.1785/BSSA0780020692.
Hough, S. E., J. M. Lees, and F. Monastero (1999). Attenuation and source properties at the Coso Geothermal Area, California, *Bull. Seismol. Soc. Am.* **89,** no. 6, 16061619, doi: 10.1785/BSSA0890061606.
Humphrey, J. R., and J. G. Anderson (1992). Shear-wave attenuation and site response in Guerrero, Mexico, *Bull. Seismol. Soc. Am.* **81,** no. 4, 1622–1645, doi: 10.1785/BSSA0820041622.
IRIS (n.d.). Community near-fault observatory, available at https://www.iris.edu/hq/initiatives/near_fault (last accessed November 2022).

Ito, E., K. Nakano, F. Nagashima, and H. Kawase (2020). A method to directly estimate S-wave site amplification factor from horizontal-to-vertical spectral ratio of earthquakes (eHVSRs), *Bull. Seismol. Soc. Am.* **110,** no. 6, 2892–2911, doi: 10.1785/0120190315.

Jachens, R. C., R. W. Simpson, R. W. Graymer, C. M. Wentworth, and T. M. Brocher (2006). Three-dimensional geologic map of northern and central California: A basic model for supporting earthquake simulations and other predictive modeling (abstract), *Seismol. Res. Lett.* **77,** 270.

Ji, C., A. Cabas, F. Bonilla, and C. Gélis (2022). Variability in kappa (κ_r): Contributions from the computation procedure, *Proc. of the Geo-Congress 2022 GSP 334*, Charolotte, North Carolina, 20–23 March.

Ji, C., A. Cabas, L. F. Bonilla, and C. Gélis (2021). Effects of nonlinear soil behavior on kappa (κ): Observations from the KiK-Net database, *Bull. Seismol. Soc. Am.* **111,** no. 4, 2138–2157, doi: 10.1785/0120200286.

Johnson, C. W., D. Kilb, A. Baltay, and F. Vernon (2020). Peak ground velocity spatial variability revealed by dense seismic array in southern California, *J. Geophys. Res.* **125,** no. 6, 1–17, doi: 10.1029/2019JB019157.

Kilb, D., G. Biasi, J. Anderson, J. Brune, Z. Peng, and F. L. Vernon (2012). A comparison of spectral parameter kappa from small and moderate earthquakes using southern California ANZA seismic network data, *Bull. Seismol. Soc. Am.* **102,** no. 1, 284–300, doi: 10.1785/0120100309.

King, E., A. Klimasewski, V. Sahakian, and A. Baltay (2019). Source and site spectral inversion for κ_0 computation in the Bay Area (abstract), *Proc. of the 2019 SCEC Annual Meeting*, Poster 001, 8–11 September.

Klimasewski, A., V. Sahakian, A. Baltay, J. Boatwright, J. B. Fletcher, and L. M. Baker (2019). κ0 and broadband site spectra in southern California from source model-constrained inversion, *Bull. Seismol. Soc. Am.* **109,** no. 5, 1878–1889, doi: 10.1785/0120190037.

Klimasewski, A., V. Sahakian, and A. Thomas (2021). Comparing artificial neural networks with traditional ground-motion models for small-magnitude earthquakes in Southern California, *Bull. Seismol. Soc. Am.* **111,** no. 3, 1577–1589, doi: 10.1785/0120200200.

Kneib, G., and S. A. Shapiro (1992). Attenuation by scattering: Theory and numerical results, *SEG Technical Program Expanded Abstracts*, 1304–1308.

Krischer, L. (2016). mtspec Python wrappers v0.3.2 [Data set], *Zenodo*, doi: 10.5281/zenodo.321789.

Ktenidou, O.-J. (2022). Hard as a rock? Reconsidering rock-site seismic response and reference ground motions, in *Progresses in European Earthquake Engineering and Seismology, ECEES*, R. Vacareanu and C. Ionescu (Editors), Springer Proceedings in Earth and Environmental Sciences, Springer, Cambridge, United Kingdom, doi: 10.1007/978-3-031-15104-0_3.

Ktenidou, O.-J., N. A. Abrahamson, R. B. Darragh, and W. J. Silva (2016). A methodology for the estimation of kappa (κ) from large datasets: Example application to rock sites in the NGA-East database and implications on design motions, *PEER Rept. 2016/01*, Pacific Earthquake Engineering Research Center, University of California, Berkeley, California.

Ktenidou, O.-J., and C. Van Houtte (2012). Empirical estimation of kappa from rock velocity profiles at the Swiss NPP Sites (19.02.2012), *Rept. TP2-TB-1090, PEGASOS Refinement Project*.

Ktenidou, O.-J., N. A. Abrahamson, S. Drouet, and F. Cotton (2015). Understanding the physics of kappa (κ): Insights from a downhole array, *Geophys. J. Int.* **203,** no. 1, 678–691, doi: 10.1093/gji/ggv315.

Ktenidou, O.-J., F. Cotton, N. A. Abrahamson, and J. G. Anderson (2014). Taxonomy of κ: A review of definitions and estimation approaches targeted to applications, *Seismol. Res. Lett.* **85,** no. 1, 135–146, doi: 10.1785/0220130027.

Ktenidou, O.-J., S. Drouet, N. Theodulidis, M. Chaljub, S. Arnaouti, and F. Cotton (2012). Estimation of kappa (κ) for a sedimentary basin in Greece (EUROSEISTEST)—Correlation to site characterisation parameters, *Proc. of the 15th World Conf. of Earthquake Engineering*, Lisbon, Portugal, 4–28 September.

Ktenidou, O.-J., C. Gélis, and L. F. Bonilla (2013). A study on the variability of Kappa (κ) in a Borehole: Implications of the computation process, *Bull. Seismol. Soc. Am.* **103,** no. 2A, 1048–1068, doi: 10.1785/0120120093.

Landwehr, N., N. M. Kuehn, T. Scheffer, and N. Abrahamson (2016). A nonergodic ground-motion model for California with spatially varying coefficients, *Bull. Seismol. Soc. Am.* **106,** no. 6, 2574–2583, doi: 10.1785/0120160118.

Laurendeau, A., F. Cotton, O.-J. Ktenidou, L. F. Bonilla, and F. Hollender (2013). Rock and stiff-soil site amplification: Dependency on VS30 and Kappa (κ0), *Bull. Seismol. Soc. Am.* **103,** no. 6, 3131–3148, doi: 10.1785/0120130020.

Lees, J., and G. Lindley (1994). Three-dimensional attenuation tomography at Loma Prieta: Inverting t* for Q, *J. Geophys. Res.* **99,** no. B4, 6843–6863, doi: 10.1029/93JB03460.

Lermo, J., and F. J. Chávez-García (1993). Site effect evaluation using spectral ratios with only one station, *Bull. Seismol. Soc. Am.* **83,** no. 5, 1574–1594, doi: 10.1785/BSSA0830051574.

Li, Y.-G., and T.-L. Teng (1990). Observation and analysis of trapped modes in the San Andreas Fault zone, *SEG Annual Meeting*. San Francisco, California, 23–27 September.

Li, Y.-G., R. D. Catchings, and M. R. Goldman (2016). Subsurface fault damage zone of the 2014 Mw 6.0 South Napa, California, earthquake viewed from fault-zone trapped waves, *Bull. Seismol. Soc. Am.* **106,** no. 6, 2747–2763, doi: 10.1785/0120160039.

Li, Y.-G., J. E. Vidale, and E. S. Cochran (2004). Low-velocity damaged structure of the San Andreas Fault at Parkfield from fault zone trapped waves, *Geophys. Res. Lett.* **31,** no. 12, 1–5, doi: 10.1029/2003GL019044.

Mai, P. M., W. Imperatori, and K. B. Olsen (2010). Hybrid broadband ground-motion simulations: Combining long-period deterministic synthetics with high-frequency multiple s-to-s backscattering, *Bull. Seismol. Soc. Am.* **100,** no. 5A, 2124–2142, doi: 10.1785/0120080194.

McPhillips, D. F., J. A. Herrick, S. Ahdi, A. K. Yong, and S. Haefner (2020). Updated compilation of VS30 data for the United States, *U.S. Geol. Surv. Data Release*, doi: 10.5066/P9H5QEAC.

Motazedian, D., and G. M. Atkinson (2005). Stochastic finite-fault modeling based on a dynamic corner frequency, *Bull. Seismol. Soc. Am.* **95,** no. 3, 995–1010, doi: 10.1785/0120030207.

Northern California Earthquake Data Center (2014). Berkeley digital seismic network (BDSN) [Data set], Northern California Earthquake Data Center, doi: 10.7932/BDSN.

Nye, T. A., V. J. Sahakian, E. King, A. Baltay, and A. Klimasewski (2022a). Estimates of kappa in the San Francisco Bay Area, *Proc.*

of the 12th National Conf. Earthquake Engineering, Earthquake Engineering Research Institute, Salt Lake City, Utah, 27 June–1 July.

Nye, T. A., V. J. Sahakian, E. King, A. Baltay, and A. Klimasewski (2022b). San Francisco Bay area kappa v1.0 [Data set], *Zenodo*, doi: 10.5281/zenodo.6040055.

Olsen, K. B., S. M. Day, J. B. Minster, Y. Cui, A. Chourasia, M. Faerman, R. Moore, P. Maechling, and T. Jordan (2006). Strong shaking in Los Angeles expected from southern San Andreas earthquake, *Geophys. Res. Lett.* **33,** no. 7, 2–5, doi: 10.1029/2005GL025472.

Ostermeijer, G. A., T. M. Mitchell, F. M. Aben, M. T. Dorsey, J. Browning, T. K. Rockwell, J. M. Fletcher, and F. Ostermeijer (2020). Damage zone heterogeneity on seismogenic faults in crystalline rock; a field study of the Borrego Fault, Baja California, *J. Struct. Geol.* **137,** doi: 10.1016/j.jsg.2020.104016.

Pacific Earthquake Engineering Research Center (2013). NGA-West2 database flatfile [Data set], *UC Berkeley*, available at https://apps.peer.berkeley.edu/assets/NGA_West2_supporting_data_for_flatfile.zip (last accessed August 2021).

Pagani, M., D. Monelli, G. Weatherill, L. Danciu, H. Crowley, V. Silva, P. Henshaw, L. Butler, M. Nastasi, L. Panzeri, *et al.* (2014). OpenQuake engine: An open hazard (and risk) software for the global earthquake model, *Seismol. Res. Lett.* **85,** no. 3, 692–702, doi: 10.1785/0220130087.

Palmer, S. M., and G. M. Atkinson (2020). The high-frequency decay slope of spectra (kappa) for M ≥ 3.5 earthquakes on rock sites in eastern and western Canada, *Bull. Seismol. Soc. Am.* **110,** no. 2, 471–488, doi: 10.1785/0120190206.

Papageorgiou, A. S., and K. Aki (1983). A specific barrier model for the quantitative description of inhomogeneous faulting and the prediction of strong ground motion. I. Description of the model, *Bull. Seismol. Soc. Am.* **73,** no. 3, 693–722, doi: 10.1086/622062.

Parker, G. A., A. S. Baltay, J. Rekoske, and E. M. Thompson (2020). Repeatable source, path, and site effects from the 2019 M 7.1 Ridgecrest earthquake sequence, *Bull. Seismol. Soc. Am.* **110,** no. 4, 1530–1548, doi: 10.1785/0120200008.

Parolai, S., and D. Bindi (2004). Influence of soil-layer properties on κ evaluation, *Bull. Seismol. Soc. Am.* **94,** no. 1, 349–356, doi: 10.1785/0120030022.

Pilz, M., F. Cotton, R. Zaccarelli, and D. Bindi (2019). Capturing regional variations of hard-rock attenuation in Europe, *Bull. Seismol. Soc. Am.* **109,** no. 4, 1401–1418, doi: 10.1785/0120190023.

Powers, P. M., and T. H. Jordan (2010). Distribution of seismicity across strike-slip faults in California, *J. Geophys. Res.* **115,** no. 5, doi: 10.1029/2008JB006234.

Prieto, G. A., R. L. Parket, and F. L. Vernon (2009). A Fortran 90 library for multitaper spectrum analysis, *Comput. Geosci.* **35,** no. 8, 1701–1710, doi: 10.1016/j.cageo.2008.06.007.

Purvance, M. D., and J. G. Anderson (2003). A comprehensive study of the observed spectral decay in strong-motion accelerations recorded in Guerrero, Mexico, *Bull. Seismol. Soc. Am.* **93,** no. 2, 600–611, doi: 10.1785/0120020065.

Rodgers, A. J., A. Pitarka, R. Pankajakshan, B. Sjögreen, and N. A. Petersson (2020). Regional-scale 3D ground-motion simulations of Mw 7 earthquakes on the Hayward fault, northern California resolving frequencies 0–10 Hz and including site-response corrections, *Bull. Seismol. Soc. Am.* **110,** no. 6, 2862–2881, doi: 10.1785/0120200147.

Ross, Z. E., Y. Ben-Zion, M. C. White, and F. L. Vernon (2016). Analysis of earthquake body wave spectra for potency and magnitude values: Implications for magnitude scaling relations, *Geophys. J. Int.* **207,** no. 2, 1158–1164, doi: 10.1093/gji/ggw327.

Sahakian, V., A. Baltay, T. Hanks, J. Buehler, F. Vernon, D. Kilb, and N. Abrahamson (2018). Decomposing leftovers: Event, path, and site residuals for a small-magnitude Anza region GMPE, *Bull. Seismol. Soc. Am.* **108,** no. 5, 2478–2492, doi: 10.1785/0120170376.

Sahakian, V. J., A. Baltay, T. C. Hanks, J. Buehler, F. L. Vernon, D. Kilb, and N. A. Abrahamson (2019). Ground motion residuals, path effects, and crustal properties: A pilot study in southern California, *J. Geophys. Res.* **124,** no. 6, 5738–5753, doi: 10.1029/2018JB016796.

Sandwell, D., R. Mellors, X. Tong, M. Wei, and P. Wessel (2011). Open radar interferometry software for mapping surface deformation, *Eos Trans. AGU* **92,** no. 28, doi: 10.1029/2011EO280002.

Schulz, S. E., and J. P. Evans (2000). Mesoscopic structure of the Punchbowl Fault, Southern California and the geologic and geophysical structure of active strike-slip faults, *J. Struct. Geol.* **22,** no. 7, 913–930, doi: 10.1016/S0191-8141(00)00019-5.

Seyhan, E., and J. P. Stewart (2014). Semi-empirical nonlinear site amplification from NGAWest2 data and simulations, *Earthq. Spectra* **30,** no. 3, 1241–1256, doi: 10.1193/063013EQS181M.

Silva, W. J., and R. B. Darragh (1995). Engineering characterization of strong ground motion recorded at rock sites, *Report TR-102262*, Electric Power Research Institute, El Cerrito, California.

Silva, W., R. Darragh, N. Gregor, G. Martin, N. Abrahamson, and C. Kircher (1998). Reassessment of site coefficients and near-fault factors for building code provisions, *Technical Report Program Element II: 98-HQ-GR-1010*, Pacific Engineering and Analysis, El Cerrito, California.

Somerville, P., R. Graves, N. Collins, S. G. Song, S. Ni, and P. Cummins (2009). Source and ground motion models for Australian earthquakes, *Proc. of the 2009 Annual Conf. of Australian Earthquake Engineering Society*, Newcastle, Australia, December.

Stewart, J. P., P. Wang, D. P. Teague, and A. Vecchietti (2019). Applications of non-ergodic site response in ground motion modeling, *Proc. of the 7th International Conf. of Earthquake Geotechnical Engineering*, Rome, Italy.

Sweetkind, D. S., E. M. Taylor, C. A. McCabe, V. E. Langenheim, and R. J. McLaughlin (2010). Three-dimensional geologic modeling of the Santa Rosa Plain, California, *Geosphere* **6,** no. 3, 237–274, doi: 10.1130/GES00513.1.

Thingbaijam, K., P. Mai, and K. Goda (2017). New empirical earthquake source-scaling laws, *Bull. Seismol. Soc. Am.* **107,** no. 5, 2225–2246, doi: 10.1785/0120170017.

Thompson, E. M., D. J. Wald, and C. B. Worden (2014). A VS30 Map for California with geologic and topographic constraints, *Bull. Seismol. Soc. Am.* **104,** no. 5, 2313–2321, doi: 10.1785/0120130312.

U.S. Geological Survey (1931). United States national strong-motion network [Data set], *International Federation of Digital Seismograph Networks*, doi: 10.7914/SN/NP.

U.S. Geological Survey (2017). Quaternary fault and fold database for the United States [Data set], available at https://www.usgs.gov/natural-hazards/earthquake-hazards/faults (last accessed August 2020).

U.S. Geological Survey (2018). CenCalVM v1.1.0, [Github Repository], available at https://github.com/usgs/earthquake-cencalvm (last accessed August 2021).

U.S. Geological Survey (2020a). Libcomcat v2.0, [Github Repository], doi: 10.5066/P91WN1UQ.

U.S. Geological Survey (2020b). USGS Bay Area Velocity Model [Data Set], available at ftp://ehzftp.wr.usgs.gov/baagaard/cencalvm/database (last accessed August 2021).

U.S. Geological Survey (n.d.). Bay Area Geologic Map [Data Set], available at https://earthquake.usgs.gov/education/geologicmaps/geology.php (last accessed December 2021).

USGS Menlo Park (1967). USGS Northern California Network [Data set], *International Federation of Digital Seismograph Networks*, doi: 10.7914/SN/NC.

Van Houtte, C., S. Drouet, and F. Cotton (2011). Analysis of the origins of (Kappa) to compute hard rock to rock adjustment factors for GMPEs, *Bull. Seismol. Soc. Am.* **101,** no. 6, 2926–2941, doi: 10.1785/0120100345.

Van Houtte, C., O.-J. Ktenidou, T. Larkin, and C. Holden (2014). Hard-site κ0 (kappa) calculations for Christchurch, New Zealand, and comparison with local ground-motion prediction models, *Bull. Seismol. Soc. Am.* **104,** no. 4, 1899–1913, doi: 10.1785/0120130271.

Van Houtte, C., O.-J. Ktenidou, T. Larkin, and C. Holden (2018). A continuous map of near-surface S-wave attenuation in New Zealand, *Geophys. J. Int.* **213,** no. 1, 408–425, doi: 10.1093/GJI/GGX559.

Wells, D., and K. Coppersmith (1984). New empirical relationships among magnitude, rupture length, rupture width, rupture area, and surface displacement, *Bull. Seismol. Soc. Am.* **84,** no. 4, 974–1002, doi: 10.1785/BSSA0840040974.

Wessel, P., J. F. Luis, L. Uieda, R. Scharroo, F. Wobbe, W. H. F. Smith, and D. Tian (2019). The Generic Mapping Tools Version 6, *Geochem. Geophys. Geosys.* **20,** no. 11, 5556–5564, doi: 10.1029/2019GC008515.

Xu, B., E. M. Rathje, Y. Hashash, J. Stewart, K. Campbell, and W. J. Silva (2020). κ_0 for soil sites: Observations from KiK-net sites and their use in constraining small-strain damping profiles for site response analysis, *Earthq. Spectra* **36,** no. 1, 111–137, doi: 10.1177/8755293019878188.

Manuscript received 30 March 2022
Published online 13 December 2022